Applied Catalysis B: Environmental 264 (2020) 118479

Contents lists available at ScienceDirect

Applied Catalysis B: Environmental

journal homepage: www.elsevier.com/locate/apcatb

Gama-graphyne as photogenerated electrons transfer layer enhances photocatalytic performance of silver phosphate

Yan Lin[a,b], Haiyang Liu[c], Chunping Yang[a,b,d,*], Xin Wu[a,b], Cheng Du[a,*], Limei Jiang[a], Yuanyuan Zhong[a]

[a] Guangdong Provincial Key Laboratory of Petrochemcial Pollution Processes and Control, School of Environmental Science and Engineering, Guangdong University of Petrochemical Technology, Maoming, Guangdong, 525000, China
[b] College of Environmental Science and Engineering, Hunan University and Key Laboratory of Environmental Biology and Pollution Control (Hunan University), Ministry of Education, Changsha, Hunan, 410082, China
[c] Datang Environment Industry Group Co., Ltd, Beijing, 100097, China
[d] Hunan Province Environmental Protection Engineering Center for Organic Pollution Control of Urban Water and Wastewater, Changsha, Hunan, 410001, China

ARTICLE INFO

Keywords:
Graphyne
Ag_3PO_4-based catalyst
Photocatalysis
Photodegradation
Photogenerated electrons transfer

ABSTRACT

γ-graphyne (γ-G), as a new kind of 2D carbon allotrope that consists of sp- and sp^2-hybrid carbon atoms, has great potential in the development of highly efficient photocatalytic systems because of its unique properties. In this study, novel photocatalysts Ag_3PO_4@γ-G with excellent photocatalytic activity and photostability were successfully synthesized by a facile preparation method. The density functional theory (DFT) calculation results of Ag_3PO_4@γ-G composite, including the band charge density distributions, three-dimensional charge density difference and planar average electrostatic potential, indicated the successful construction of electrons transfer layer in Ag_3PO_4@γ-G composite. The photogenerated electrons of Ag_3PO_4 can be rapidly transferred to the γ-G under the driving of built-in potential well, which leads to the high separation efficiency of photogenerated carriers and greatly improves the photocatalytic performance of catalysts. The photocatalytic degradation rate of norfloxacin (NFL), 2-Hydroxynaphthalene (2-HNP) and phenol over the binary composite catalyst could reach 100 % only after 8, 5 and 16 min of visible light irradiation respectively, and the apparent rate constants of which were 15.3, 9.6 and 19.7 times higher than that of the pure Ag_3PO_4 respectively. The analyses of LC–MS and 3D EEMs showed that the 2-HNP and NFL mainly degraded into short-chain carboxylic acids. The results of free radical quenching experiment and ESR characterization suggested that all kinds of active species worked in the degradation process, while the photogenerated holes and superoxide radicals played a dominant role. The novel addition of γ-G and the construction of electrons transfer layer in photocatalysts provide a new strategy for the design of efficient environmental remediation catalysts.

1. Introduction

Facing the aggravating energy crisis and environment pollution, it is necessary to find environment-friendly clean energy and develop efficient treatment technology [1,2]. Semiconductor photocatalysis has become increasingly promising technology, which can directly utilize solar energy to degrade pollutants efficiently [3–5]. The core issue of this technology is to explore and construct the new photocatalyst with good stability and high photocatalytic efficiency [6–8]. Among numerous photocatalysts, silver phosphate (Ag_3PO_4) has been proved to be one of the most potential photocatalysts due to its high oxidative ability, simple preparation process and low toxicity [9]. More especially, under visible light irradiation, it can achieve about 90 % quantum efficiency in water oxidation and show excellent decomposition ability for organic pollutants [10]. However, it is also inevitably flawed. The photocorrosion is relatively severe after illumination and it tends to form large-sized crystals particles in the preparation process, which greatly limits its wide application and catalytic performance [11].

Many attempts have been made to overcome these shortcomings, including the preparation of small-sized crystal particles [12,13], facet engineering and shape control [10,14], and the construction of heterogeneous structures [11,15]. Assembling Ag_3PO_4 with other materials to form composite photocatalysts exhibits the unique advantages of

---

* Corresponding authors at: School of Environmental Science and Engineering, Guangdong University of Petrochemical Technology, Maoming, Guangdong, 525000, China.

E-mail addresses: yangc@hnu.edu.cn (C. Yang), ducheng@gdupt.edu.cn (C. Du).

https://doi.org/10.1016/j.apcatb.2019.118479
Received 4 November 2019; Received in revised form 25 November 2019; Accepted 27 November 2019

improving the optical absorption performance, effectively separating and transferring charges, and enhancing the stability [16]. At present, the main composite agents are metal [17], semiconductor [18], polymer [19] and carbon materials [20]. Among them, the addition of carbon materials has been proved to be a very effective method to optimize the microstructure of Ag_3PO_4 and improve its photocatalytic performance [9]. For example, Yang et al. used the graphene to fabricate Ag_3PO_4-graphene composite photocatalyst, which greatly improved the photocatalytic performance and stability of Ag_3PO_4 [20]. The combination of carbon quantum dots and Ag_3PO_4 was also an ideal strategy for the preparation of stable and efficient complex photocatalytic [21]. Our previous reports indicated that the coupling of MWCNTs could not only enhance the catalytic activity of Ag_3PO_4, but also control its crystal size [22,23]. The above successful cases fully demonstrated that carbon material is a promising candidate to overcome the defects of Ag_3PO_4 and improve its catalytic performance.

Graphynes is one kind of new carbon allotropes that feature layered 2D structure assembled by carbon atoms with sp- and sp^2- hybridization form [24,25]. The presence of acetylenic groups in graphynes generates more excellent optical and electronic properties than those of conventional carbon materials [26]. In the past few decades, many efforts including theoretical predictions and practical experiments have been carried out to explore this novel material. Until 2010, Li et al. synthesized graphdiyne films on the surface of copper via a cross-coupling reaction using hexaethynylbenzene for the first time [27]. Graphynes can be classified as α-graphyne, β-graphyne, γ-graphyne, 6,6,12-graphyne, graphdiyne and so on. In the graphyne family, γ-graphyne (γ-G) possesses the highest stability in theory, and there is an acetylenic group between the two adjacent hexagons benzene rings [28]. Moreover, Puigdollers et al. reported that γ-G has high-velocity carrier transport capacity [29]. Therefore, the application of γ-G in the field of photocatalysis has also been developed. For instance, γ-G was combined with TiO_2 to fabricate the TiO_2/γ-G heterojunction structure, indicating that the addition of γ-G can simultaneously improve the absorption of visible light and suppress the recombination of photoexcited electron-hole pairs during the photocatalytic process [28]. Yang et al. also found that compared with the pure TiO_2 and TiO_2/graphene, the TiO_2/graphyne composite exhibited the most outstanding performance in the charge separation and oxidation ability [30]. The above reports showed that γ-G is a good additive for photocatalytic system, which can effectively inhibit the recombination of carriers and improve the photocatalytic activity.

Despite the excellent properties of γ-G, it is difficult to produce in large scale through the cross-coupling reaction using hexaethynylbenzene due to its sophisticated preparation process and harsh conditions. Thus, it is urgent to find a simpler synthetic method. Mechanochemistry has been regarded as a driving force for cross-coupling reaction. Li et al. synthesized some alkynyl carbon materials by interfacial mechanochemical reactions [31]. Turberg et al. prepared the 1,4-diamino-2-butynes by mechanochemical method with calcium carbide as acetylene source [32]. More specially, Cui et al. successfully synthesized the γ-G by cross-coupling reaction using calcium carbide and 1,3,5-tribromobenzene via mechanochemistry [25,33]. Thus, it is feasible to prepare γ-G by this simple, rapid and reproducible chemical synthesis method.

Based on the previous works, the γ-G with high-speed carrier mobility is considered as a promising photogenerated electrons transfer layer to transfer the photogenerated electrons of Ag_3PO_4 rapidly to the surface of catalyst, inhibit the photocorrosion and improve its photocatalytic activity. However, to the best of our knowledge, there is little information about the novel Ag_3PO_4@γ-G composite photocatalyst with superior photocatalytic performance and photostability. No previous reports have appeared regarding the use of facile preparation method that combined the mechanochemistry and electrostatically driven self-assembly approach to fabricate the γ-G-based photocatalyst. Moreover, the reports and data proof on the construction of electrons transfer layer in Ag_3PO_4-based photocatalyst are not available. Herein, the novel photocatalyst Ag_3PO_4@γ-G was synthesized for the first time by a facile method. In addition, the photogenerated electrons transfer layer in Ag_3PO_4@γ-G composite was constructed and proved firstly by the DFT calculation. The photocatalytic performance of photocatalysts was evaluated by degradation of norfloxacin (NFL), 2-Hydroxynaphthalene (2-HNP) and phenol under visible light. The photodegradation products and pathway of NFL and 2-HNP were investigated by the LC–MS and 3D EEMs. The photodegradation mechanisms were studied by the free radical quenching experiment and ESR characterization. This study proposed a new design strategy for improving the carrier separation efficiency and developing Ag_3PO_4-based photocatalyst.

2. Experimental section

2.1. Chemicals and materials

Norfloxacin (NFL) and 2-Hydroxynaphthalene (2-HNP) were purchased from Sigma-Aldrich. Phenol, benzene, ethanol, glacial acetic acid, triethylamine, silver nitrate ($AgNO_3$), disodium hydrogen phosphate dodecahydrate ($Na_2HPO_4·12H_2O$), calcium carbide (CaC_2) and nitric acid (HNO_3) were purchased from Sinopharm Chemical Reagent Co., Ltd. (Shanghai, China). All the reagents were of analytical grade, and de-ionized water (18.25 MΩ.cm) was used in the whole experiment.

2.2. Preparation of samples

2.2.1. Synthesis of γ-graphyne

The preparation of γ-graphyne was referred to a modified mechanochemical method [33,34]. Typically, 2 mL of benzene, 10.0 g of CaC_2, 35 mL of ethanol and 375 g of stainless steel balls with different diameters (5, 8, 10, 12 and 15 mm) were mixed in a stainless steel pot (250 mL). The pot was processed in planetary ball mill (TENCAN QXQM-2, China) under vacuum condition. The precursor compounds were ball-milled at 600 rpm for 8 h, and then at 450 rpm for 8 h. To avoid overheating, a cooling interval of 3 min was set after every 6 min during the milling. After then, the obtained products were annealed in N_2 flow at 260 °C for 3 h. The annealed powder was purified twice by HNO_3 (0.1 mol/L) and glacial acetic acid (2 mol/L) with ultrasonic treatment for 1 h, respectively. Finally, the obtained samples collected from the above dispersions were washed repeatedly with deionized water to neutral and dry in vacuum (60 °C).

2.2.2. Synthesis Ag_3PO_4 of and Ag_3PO_4@γ-graphyne (Ag_3PO_4@γ-G)

The synthetic method of pure Ag_3PO_4 and Ag_3PO_4@γ-G was referred to our previously reported methods [23]. Typically, the Ag_3PO_4@γ-G was prepared by an electrostatically driven self-assembly method. Firstly, 0.01 g γ-G were dispersed into deionized water (400 mL), and sonicated for 1 h to get a γ-G suspension. Secondly, γ-G suspension with different volumes was diluted to 100 mL, and $AgNO_3$ solution dissolved by 1.074 g $AgNO_3$ in 20 mL de-ionized water was added to the above γ-G aqueous suspension at a rate of 0.3 mL/min. The mixture was stirred in dark for 12 h. Then, $Na_2HPO_4·12H_2O$ solution (20 mL, 3 mmol) was added to the mixture of $AgNO_3$ and γ-G at the rate of 0.1 mL/min, and stirred for 6 h under dark conditions. Finally, the precipitate was washed with deionized water and ethanol for several times, and dried in vacuum (55℃). For comparison, the pure Ag_3PO_4 was prepared under the same conditions as Ag_3PO_4@γ-G without γ-G.

2.3. Computational methods

All calculations were performed using the MedeA-VASP package. The calculation was based on the density functional theory (DFT) and the GGA-PBE exchange-correlation functional for describing the interactions. Van der Waals interactions were added by means of a forcefield

(DFT + D3 approach of S. Grimme with zero-damping). Since no magnetic moments were in the model, this was a non-magnetic calculation using 'normal' precision and an increased planewave cutoff energy of 520.00 eV. The electronic iterations convergence was 1.0^{-5} eV using the normal (blocked Davidson) algorithm and real space projection operators. The requested k-spacing is 0.3 per Angstrom, which leads to a $2 \times 2 \times 1$ mesh. This corresponds to actual k-spacings of $0.261 \times 0.251 \times 0.209$ per Angstrom. The k-mesh was forced to be centered on the gamma point, using Gaussian smearing with a width of 0.05 eV. The GGA-PBE functional to describe the approximate exchange-correlation potential leads to a vast underestimation of the band gap, which is due to the self-interaction error inherent to this functional. Thus, the calculations of band structure were based on the hybrid functional HSE06 for describing the interactions, and non-local exchange was evaluated using 'Fast' precision. The Ag_3PO_4 (100) surface was chosen to model the Ag_3PO_4, because it is the most stable one among the low index surfaces [9,23]. In a supercell ($12.03 \times 12.53 \times 30$ Å^3), a single γ-G layer containing 48 carbon atoms sits on the Ag_3PO_4 (100) surface slab containing 128 atoms with the several bottom layers fixed at bulk position. The vacuum depth was as large as 15 Å for all of the models to avoid artificial interaction. The models of different samples were presented in Fig. S1.

The section of characterization and photocatalytic experiments are provided in the supporting information.

3. Results and discussion

3.1. Characterization of materials

The morphologies and microstructures of γ-G were characterized by SEM and HRTEM (Fig. 1). As shown in Fig. 1a, as-prepared γ-G presented as the 2D multilayer thin flake structure with rough surface, and there were a small amount of flaky structure that exhibited as curling feature. The TEM image (Fig. 1b, c) also indicated clear overlapped sheet morphology of the prepared sample, which further confirmed the 2D morphology of γ-G. The selected area electron diffraction (SAED) pattern indicated that the material with polycrystallinity (Fig. 1d). The corresponding lattice distances were determined and calculated as 0.298, 0.223 and 0.153 nm, respectively. According to previous reports, layered graphyne has various stacked crystalline structures, including the AA, AB, and ABC stacking modes [35,36]. In addition, the corresponding lattice distances of γ-G with AA/AB stacking mode could be calculated as 0.198, 0.224, 0.297 and 0.342 nm, respectively [29,33]. Thus, the lattice distances of as-prepared γ-G coincided well with the AA/AB stacking mode. Moreover, the lattice fringes spacing of 0.365 and 0.223 nm could be clearly seen in the image of HRTEM (Fig. 1e and f). The lattice parameter of 0.365 nm was in good agreement with the spacing between carbon layers [37]. The typical interplanar spacing of 0.223 nm observed in the Fig. 1f further indicated that as-prepared sample was the γ-G with AA/AB stacking mode. The corresponding fast Fourier transform (FFT) pattern (inset image in Fig. 1f) indicated that the γ-G presented as a hexagonal pattern, which is the typical pattern of hexagonal crystal system [35]. This was consistent with the crystal structure of graphyne.

The atomic force microscopy (AFM) was performed to obtain more information about the 2D morphology and layer structure of the prepared γ-G. The results were provided in Fig. 2A, it could be found that the γ-G showed flake structure with a thickness about of 1.4–1.5 nm, indicating as-prepared material was about four layers (≈ 0.365 nm × 4). The bonding structure and chemical environment of the element in γ-G were investigated by XPS and Raman spectroscopy. As shown in Fig. 2B, the high-resolution C1 s XPS spectra were corrected by Shirley background and fitted by Lorentzian and Gaussian functions, which could be deconvoluted into four subpeaks. Peaks located at 284.5, 285.2, 286.7 and 288.5 eV were attributed to the sp^2 (C = C), sp (C≡C), C—O, and C = O respectively [36,38]. The presence of O signal was due to the absorption of air in γ-G [37]. Interestingly, it could be observed that the abundance ratio of the sp^2/sp hybrid carbons was about 1.0, which was in good agreement with the chemical composition of γ-G [25]. Two kinds of hybrid carbons with excellent symmetry area ratio indicated that as-prepared material possessed high structural integrity [28,33]. The Raman spectrum of γ-G was provided in the Fig. 2C. The band at around 681 cm^{-1} could attribute to the bending vibration of sp-hybridized carbon that originated from the conjugated ethynyl links [34]. The characteristic peaks located at 1346 cm^{-1} and 1578 cm^{-1} corresponded to the D bands and G bands, which were attributed to the amorphous carbon and aromatic rings carbon, respectively [39]. The peaks at 1942 and 2190 cm^{-1} were due to the stretching vibration of alkynyl groups (—C≡C—), which further confirmed the presence of sp hybrid carbon [24]. The above characterization results indicated that the γ-G with high structural integrity have been successfully prepared, and its chemical structure as shown in Fig. 2D.

To acquire the morphology and microstructure information of Ag_3PO_4 and Ag_3PO_4@γ-G, as-prepared samples were firstly characterized by SEM and element mapping. As shown in Fig. 3a, pure Ag_3PO_4 crystal was an irregular spherical polyhedron with a diameter of about 10 − 20 μm, and some small particles were attached to it. Interestingly, after coupling with the γ-G, no large Ag_3PO_4 crystal particles could be found in the Ag_3PO_4@γ-G composite, and the particle size of Ag_3PO_4 ranged from 0.1 to 0.4 μm (Fig. 3b). Similar phenomena have been reported in our previous studies, which were due to the electrostatically driven assembly between the positively charged Ag^+ and the negatively charged γ-G [13,20,22]. Moreover, as presented in the SEM images of Ag_3PO_4@γ-G composite (Fig. 3c–d), flake γ-G were clearly seen and in good contact with the Ag_3PO_4 particles. In order to further observe the distribution of γ-G in the composites, SEM-elemental mapping images were provided in Fig. 3e–i, indicating that γ-G were evenly distributed in the Ag_3PO_4@γ-G composite. To acquire more structural information, the HRTEM image of different samples was recorded and presented in Fig. 4. The overlapped structure of flake was γ-G, and the Ag_3PO_4 particles were coated by the sheet or attached to the sheet. The typical lattice fringes distance of 0.224 nm belonged to the γ-G could be clearly observed in Fig. 4b and d. The interplanar spacing of 0.268 and 0.245 nm were also found in the HRTEM image of Fig. 4d and f, which correspond to the (210) and (211) crystal planes of Ag_3PO_4, respectively (JCPDS No.06-0505). The above results indicated that the γ-G were successfully introduced into Ag_3PO_4@γ-G composite, and the good binding between Ag_3PO_4 and γ-G was built.

The X-ray diffraction (XRD) pattern (Fig. 5a) clearly indicated that all of the diffraction peaks of the Ag_3PO_4 and Ag_3PO_4@γ-G composite could be readily indexed to the body-centered cubic structure of Ag_3PO_4 (JCPDS No. 06-0505). No characteristic diffraction peaks for γ-G were observed in the pattern because of the fairly low amount and the relatively low diffraction intensity of γ-G [20]. The positions of diffraction peaks for Ag_3PO_4 in different samples were almost the same. However, it was worth noting that obvious changes in the intensity ratios for various peaks were observed. More specifically, in the case of Ag_3PO_4@γ-G, the intensity ratio of 1.21 for the (222) and (110) diffractions was remarkably higher than the intensity ratio (0.847) of Ag_3PO_4, confirming that the content of {111} crystalline planes in the composite was obviously higher than that in Ag_3PO_4. According to previous report, the surface energy of Ag_3PO_4 {111} facet (1.65 J/m^2) was much higher than that of {110} (0.78 J/m^2) [10]. The photocatalyst with higher surface energy facets will show better photocatalytic activity [9,10]. Therefore, the introduction of γ-G was beneficial to the optimization of Ag_3PO_4 crystal facets exposure and the improvement of catalytic activity of Ag_3PO_4.

XPS analyses were performed to investigate the elemental chemical state and the interaction between Ag_3PO_4 and γ-G. It could be found that the γ-G was composed of carbon, and the signals of C, Ag, P and O were all detected in the XPS spectra of Ag_3PO_4@γ-G composites (Fig.

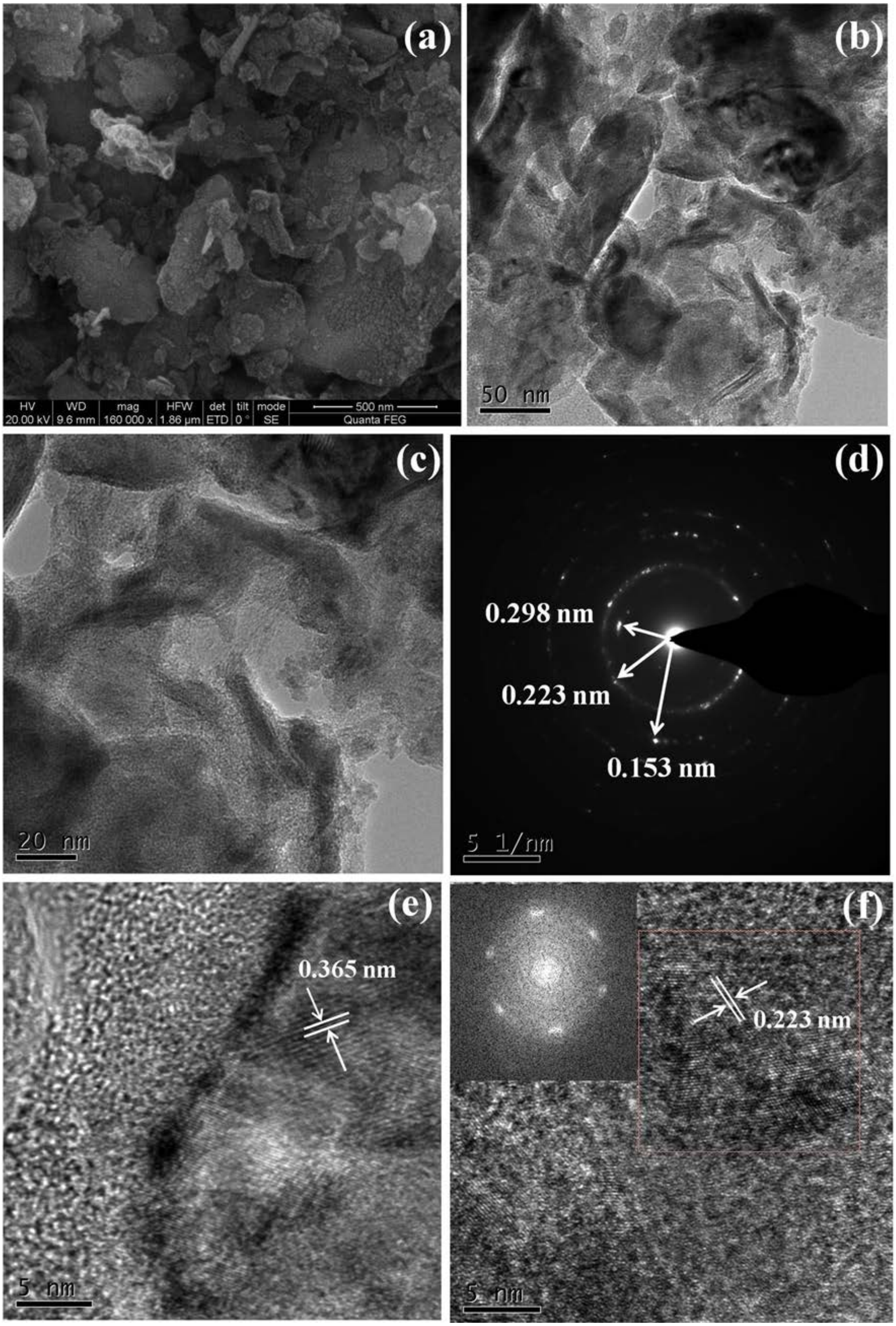

Fig. 1. SEM (a), TEM (b,c), SAED (d) and HRTEM images analysis (e–f) of γ-G.

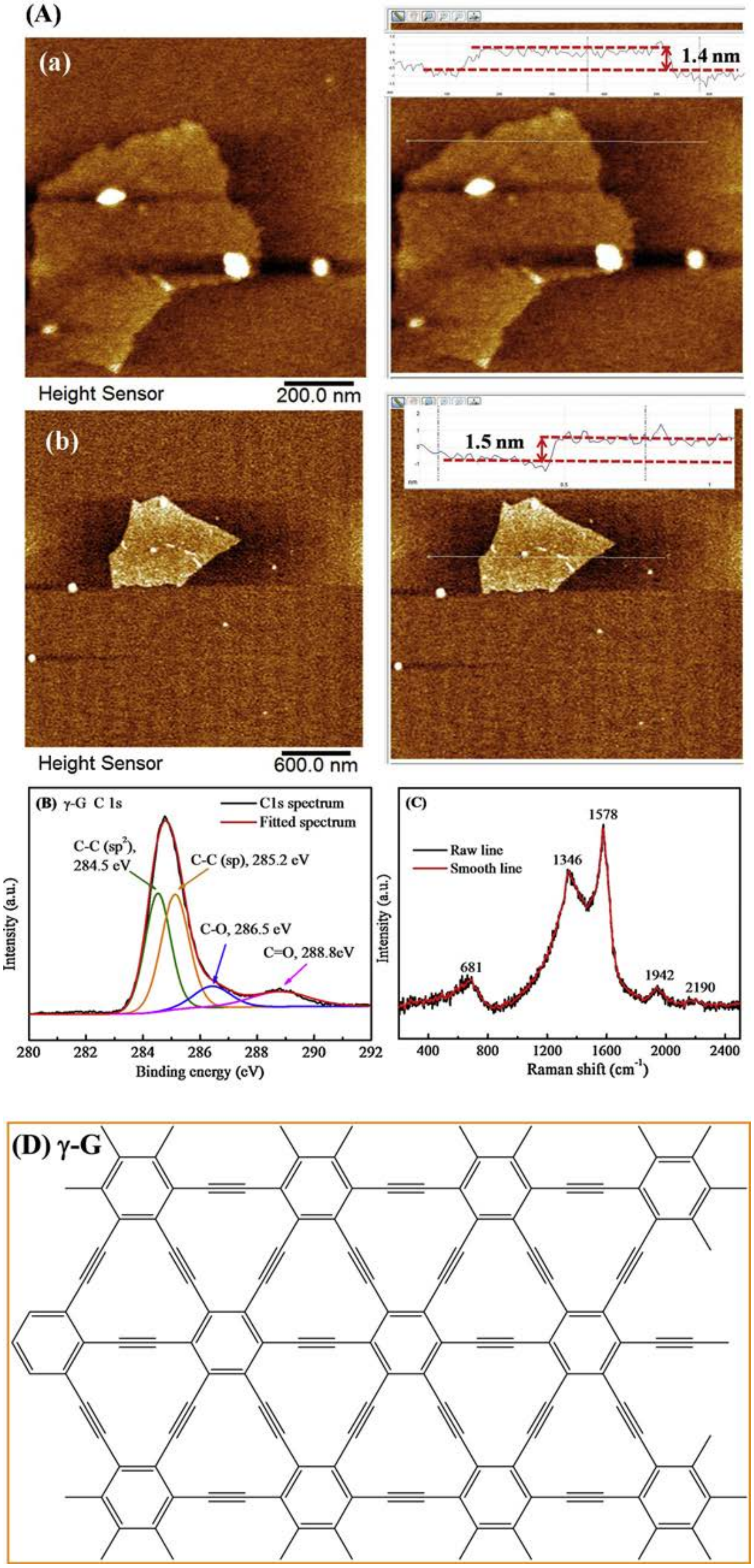

Fig. 2. AFM image analysis (A), high resolution C 1s XPS spectrum (B), Raman spectrum of γ-G (C) and chemical structural formula of the γ-G (D).

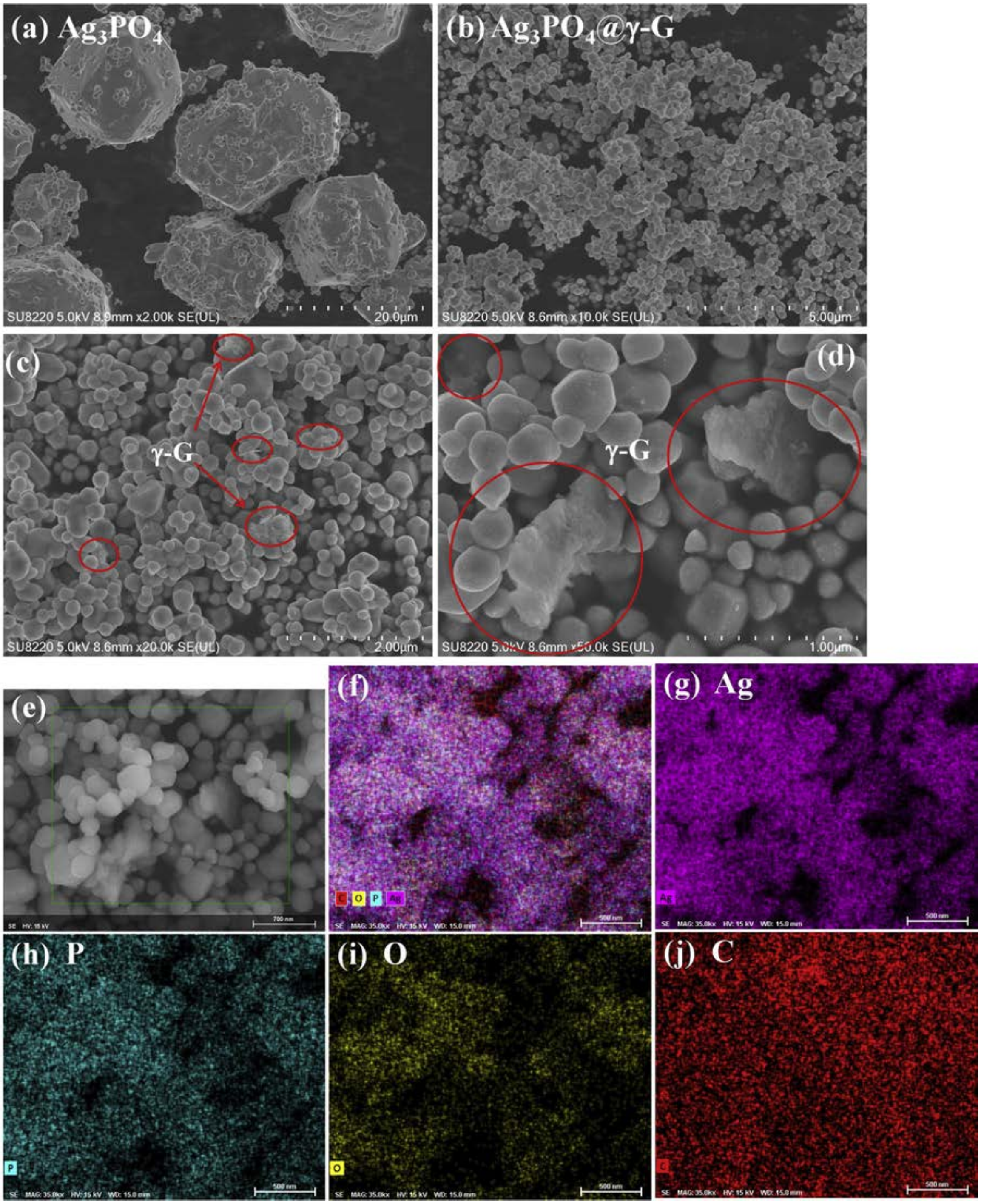

Fig. 3. SEM images of large-sized Ag_3PO_4 (a), Ag_3PO_4@γ-G (b–d) and elemental mapping images of Ag_3PO_4@γ-G composite (e–j).

S2). Fig. 5b displayed the Ag 3d spectrum. For pure Ag_3PO_4, the Ag $3d_{5/2}$ and $3d_{3/2}$ peaks were located at binding energy of 367.7 and 373.7 eV respectively, which indicated the existence of Ag^+ in the Ag_3PO_4. The typical peak of P 2p at 133.0 eV could be clearly seen in Fig. 5c, which was in agreement with the phosphorus in $PO_4{}^{3-}$. The O 1s spectrum was divided into two different peaks located at 530.5 eV and 531.9 eV, respectively (Fig. 5d). They were attributed to the lattice oxygen and surface oxygen of Ag_3PO_4, respectively [40]. Interestingly, after coupling with the γ-G, the characteristic peaks of Ag, P and O elements in Ag_3PO_4@γ-G composite all moved to the positive position, indicating there was a strong interfacial interaction between them. In addition, the binding energy is related to the electron density on catalyst surface, so the XPS results suggested that there may be electron transfer between the interfaces of Ag_3PO_4 and γ-G [41].

UV-vis diffuse reflectance spectrum (DRS) was measured to evaluate the optical properties of as-prepared samples, and the results were presented in Fig. 6a. The spectra of Ag_3PO_4 indicated that it absorbed light with wavelengths less than 530 nm, corresponding to the band gap energy of 2.35 eV. Band gap energy was calculated by the Kubelka-Munke equation, and the detailed information was provided in supporting information (Fig. S3). Obviously, after coupling with γ-G, there was a distinct enhancement of light absorbance in the wavelength range of 300 − 800 nm, which was conducive to utilizing visible light more efficiently and improving the photocatalytic performance of catalysts.

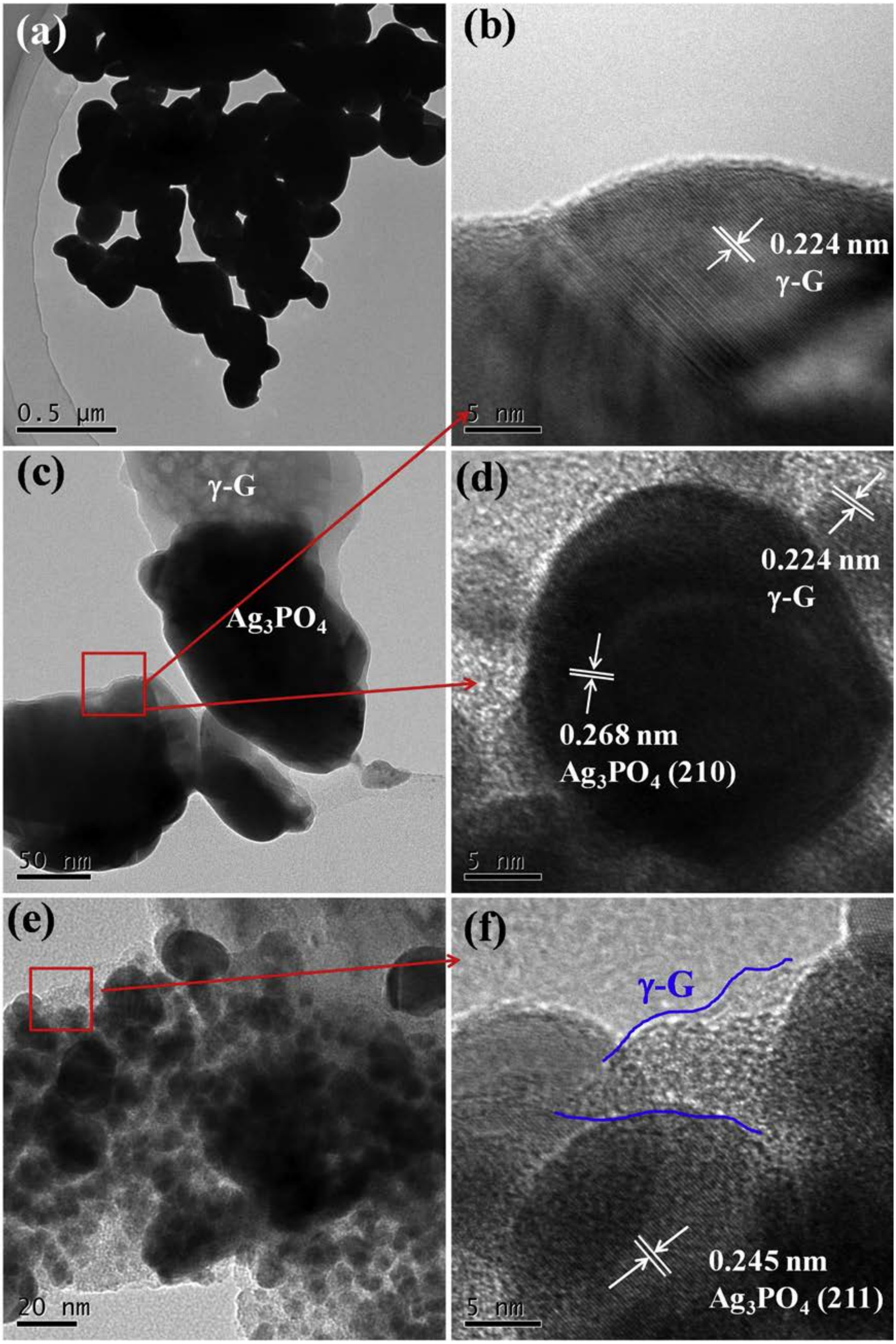

Fig. 4. HRTEM images analysis of Ag_3PO_4@γ-G.

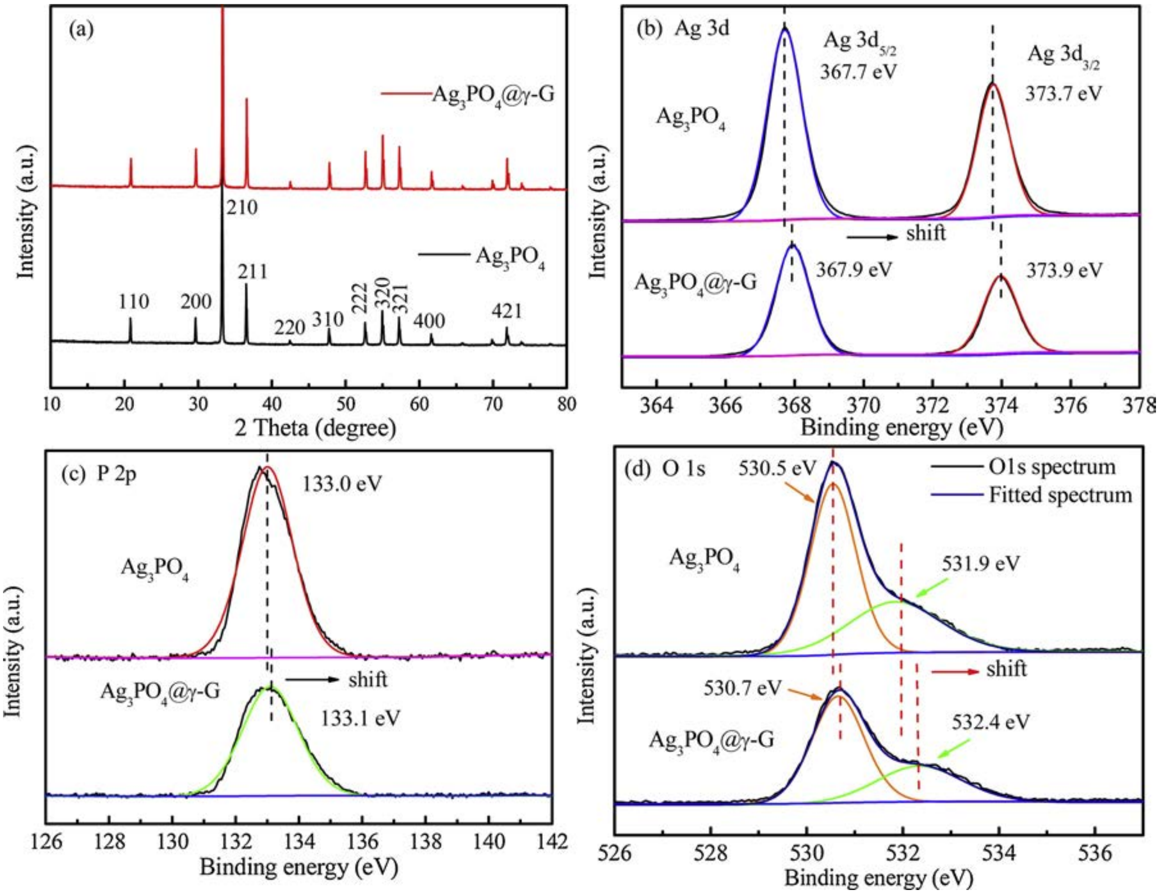

Fig. 5. XRD pattern of different samples (a), high resolution XPS spectrum of (b) Ag 3d, (c) P 2p, (d) O 1s of Ag_3PO_4@γ-G.

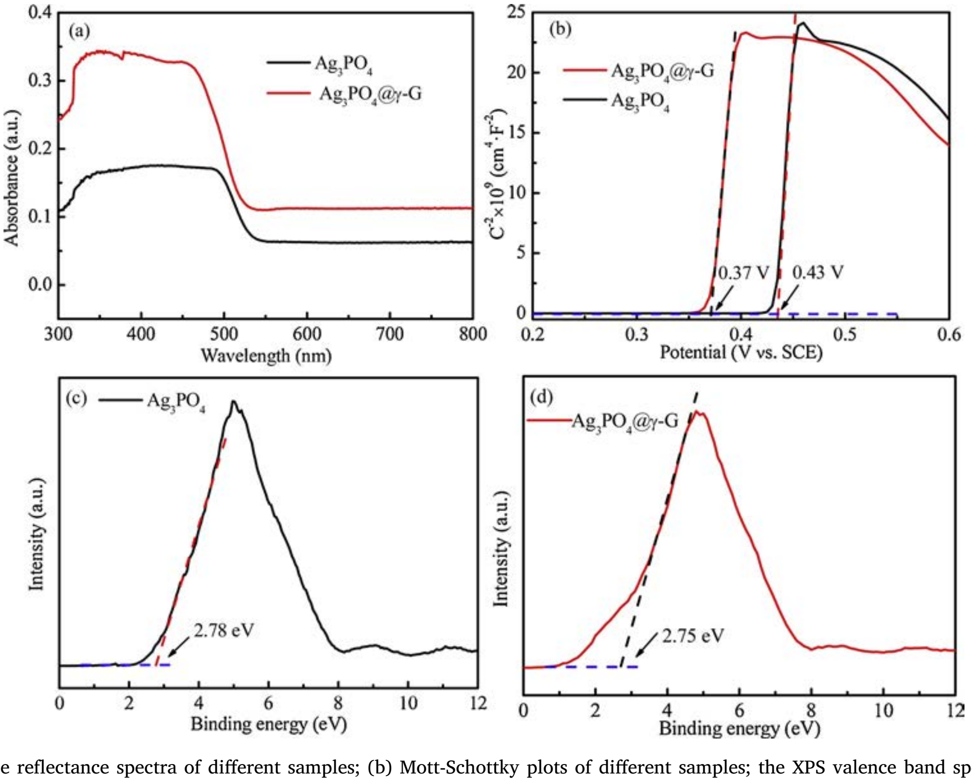

Fig. 6. (a) UV–vis diffuse reflectance spectra of different samples; (b) Mott-Schottky plots of different samples; the XPS valence band spectra of Ag_3PO_4 (c) and Ag_3PO_4@γ-G (d).

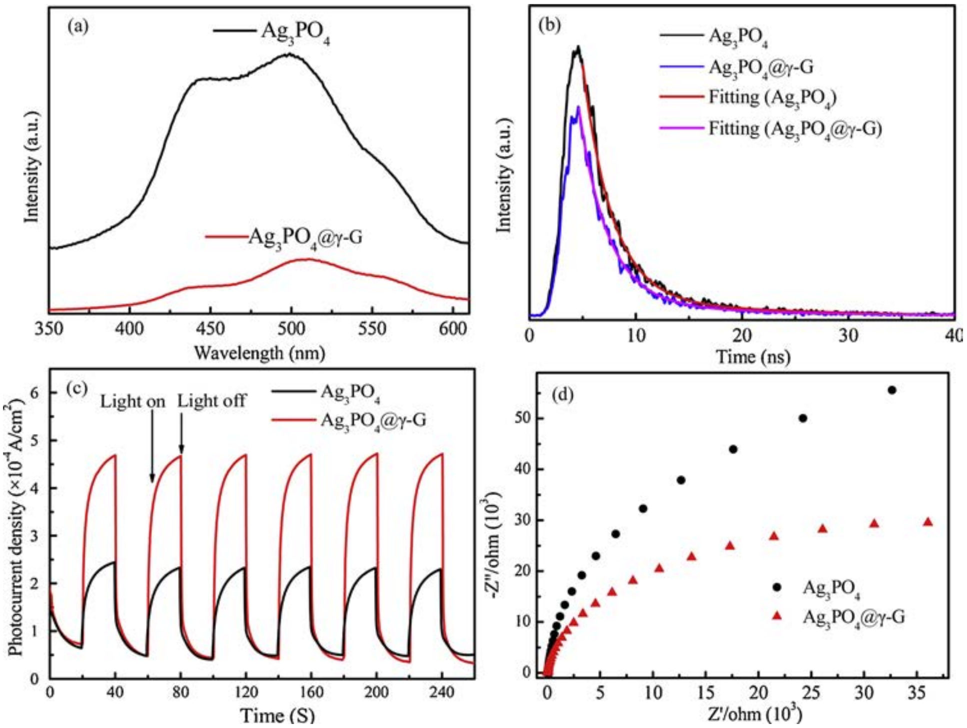

Fig. 7. (a) Photoluminescence (PL) spectra, (b) TRPL decay spectra, (c) photocurrent response density and (d) EIS Nyquist plots of as-prepared samples.

Moreover, the Mott-Schottky (MS) plot was measured to estimate the flat band potential (E_{FB}). The MS plot of Ag_3PO_4 has a positive slope, indicating its n-type semiconductor nature (Fig. 6b). It could found that the applied potential (E) of Ag_3PO_4 was 0.43 V vs. SCE, so the E_{FB} was calculated as 0.40 V, which are equal to 0.64 V vs. NHE. Since the conduction band potential (E_{CB}) is generally considered to be 0.2 V lower than E_{FB}, the E_{CB} of Ag_3PO_4 could be calculated as 0.44 V vs. NHE [22]. The Eg of Ag_3PO_4 was 2.35 eV, so its valence band potential (E_{VB}) was determined as 2.79 V vs. NHE, which indicated the Ag_3PO_4 possess highly positive VB position and strong oxidation ability. Compared with pure Ag_3PO_4, the flat-band potential of $Ag_3PO_4@\gamma$-G composite has a slight negative shift (0.06 V), implying there was an electronic interaction between Ag_3PO_4 and γ-G [19]. In order to recheck the VB position, the XPS valence band spectra were also performed and the results as shown in Fig. 6c–d. The VB potential of Ag_3PO_4 was estimated to be 2.78 eV, which was in good agreement with the above calculation value. Similarly, a slight negative shift in the VB potential of $Ag_3PO_4@\gamma$-G was also found in the XPS-VB spectra (Fig. 6d).

In order to investigate the interfacial charge transfer and recombination rates for photocatalysts, the PL spectra of different samples was firstly performed. As shown in Fig. 7a, pure Ag_3PO_4 displayed the higher PL intensity. In contrast, $Ag_3PO_4@\gamma$-G composite possessed much lower PL signal. In general, lower PL signals suggest the higher separation efficiency of photogenerated electron-hole pairs [42]. This result indicated that the recombination rate of photogenerated electrons and holes pairs was efficiently inhibited through the combination of Ag_3PO_4 and γ-G. In addition, time resolved photoluminescence (TRPL) decay spectra were also employed to study the charge carrier lifetime of the samples [43]. The curves can be fitted well based on a biexponential decay function (Fig. 7b). The detailed calculation information was provided in supporting information, and the fitting parameters were summarized in Table S1. The short radiative lifetime (τ_1) of Ag_3PO_4 was 2.79 ns. After coupling with γ-G, the τ_1 was decreased to 2.66 ns. The long radiative lifetime (τ_2) of the charge carriers was 24.48 ns for Ag_3PO_4 and 11.82 ns for $Ag_3PO_4@\gamma$-G, respectively. The results indicated that the lifetime of $Ag_3PO_4@\gamma$-G was much shorter than that of Ag_3PO_4, implying that an additional nonradiative decay channel was opened through the electron transfer from Ag_3PO_4 to γ-G and effectively suppressed the recombination of photogenerated carriers [44–46]. Moreover, photocurrent response density was also performed to detect the photoresponses of pure Ag_3PO_4 and $Ag_3PO_4@\gamma$-G composite. As presented in Fig. 7c, the photocurrent intensity of the working electrode changes rapidly with the light on and off. The photocurrent densities of $Ag_3PO_4@\gamma$-G were much higher than those of pure Ag_3PO_4, indicating the separation efficiency of photogenerated carriers was obviously enhanced after the introduction of γ-G. Electrochemical impedance spectra (EIS) were also measured to further validate the enhanced charge separation efficiency. Because the smaller semicircle in the Nyquist plots indicated higher charge carrier transfer efficiency [47], more effective separation of carriers in the $Ag_3PO_4@\gamma$-G composite also could be found in the Fig. 7d. These results demonstrated that the introduction of γ-G can remarkably improve the photogenerated carrier separation efficiency of Ag_3PO_4.

3.2. Photocatalytic degradation of organic pollutants

Norfloxacin (NFL) is an effective antibiotic widely used in clinical treatment. However, its environmental residues can lead to antibiotic resistance of aquatic bacteria and potential hazards to human safety and health [48,49]. 2-Hydroxynaphthalene (2-HNP) is an important organic raw material and dye intermediate, which is widely used in industrial production and often appears in industrial wastewater. Phenol also is an important chemical compound with a large number of applications and its production is estimated to reach 6 million tons per year in China [50]. Therefore, the NFL, 2-HNP and phenol were selected as typical pollutants and as the representatives of antibiotics, polycyclic compounds and phenolic pollutants for degradation experiments.

In order to ensure the adsorption desorption equilibrium, the dark adsorption reaction was carried out before the light irradiation. As shown in Fig. 8a, the pure Ag_3PO_4 showed unsatisfactory photocatalytic activity, and only 32 % of phenol was degraded after 20 min of illumination. Compared to the Ag_3PO_4, all binary $Ag_3PO_4@\gamma$-G composites

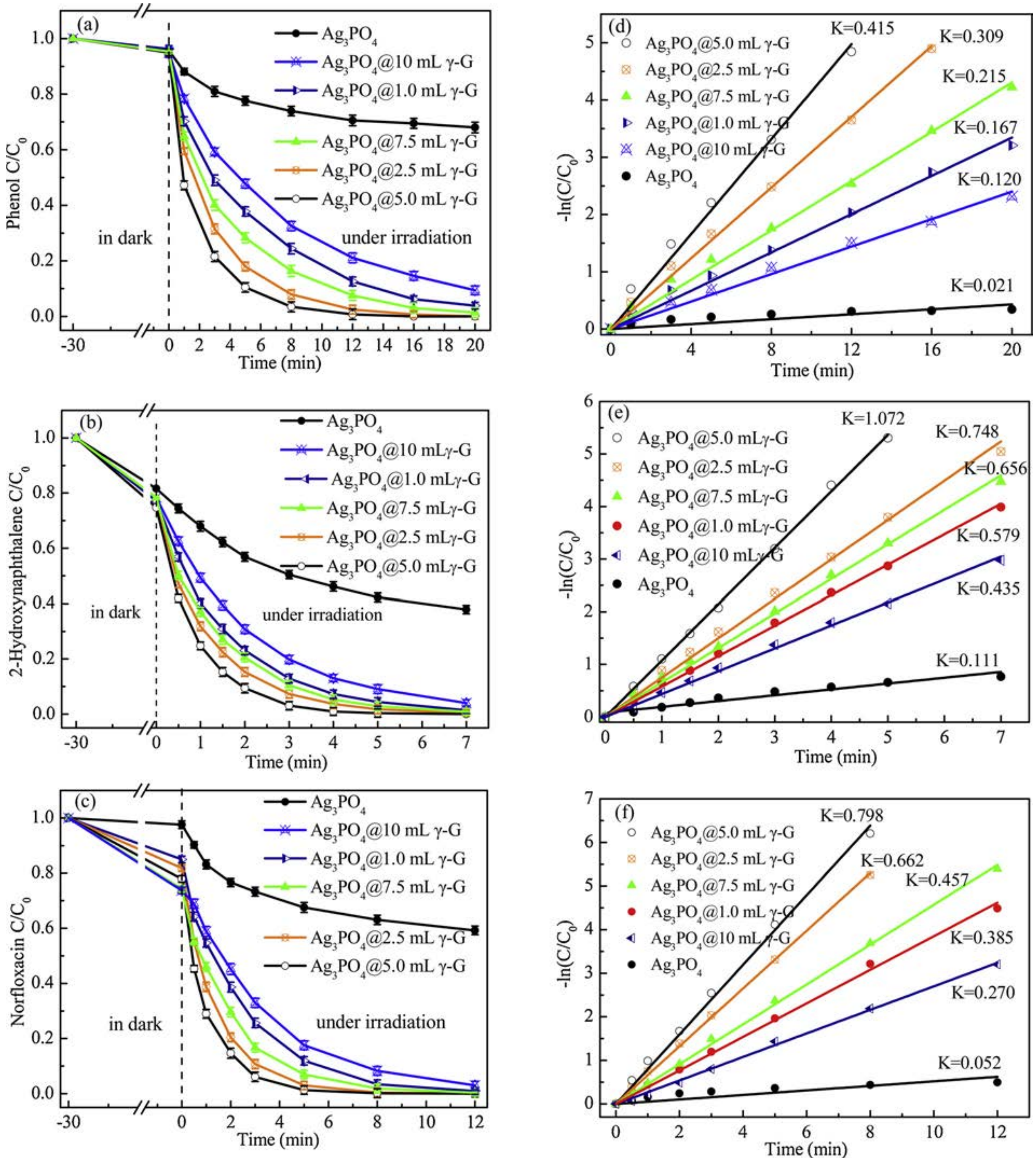

Fig. 8. Photodegradation curves of phenol (a), 2-HNP (b) and NFL (c) in the presence of as-prepared samples; Reaction kinetic curves (d,e,f) of as-prepared samples corresponding to the photodegradation curves (a,b,c), respectively.

exhibited much higher photocatalytic activity. Especially, Ag_3PO_4@5 mLγ-G catalyst achieved the highest degradation efficiency, where 100 % of phenol was removed after 16 min irradiation. To give a deep insight of the photocatalytic degradation process, the experimental results were simulated by pseudo-first-order kinetic model. As shown in Fig. 8d, the apparent rate constant for phenol degradation with Ag_3PO_4 and Ag_3PO_4@5 mLγ-G were 0.021 and 0.415 min^{-1} respectively, which increased by 19.7 times after coupling with γ-G. Furthermore, the photocatalytic activity of as-prepared photocatalysts was also evaluated by the degradation of 2-HNP. As shown in Fig. 8b, the Ag_3PO_4@5 mLγ-G composite still exhibited the highest photocatalytic activity, which could remove 100 % of 2-HNP within 5 min. The apparent rate constant of Ag_3PO_4@5 mLγ-G composite (1.072 min^{-1}) was about 9.6 times higher than that of pure Ag_3PO_4 (0.111 min^{-1}) (Fig. 8e). Not surprisingly, the binary photocatalysts still exhibited excellent catalytic activity for the degradation of NFL (Fig. 8c). The rate constant for the NFL degradation was greatest for Ag_3PO_4@5 mLγ-G (0.798 min^{-1}), which was about 15.3 times than that of pure Ag_3PO_4 (0.052 min^{-1}) (Fig. 8f). Moreover, the HPLC chromatogram of phenol, 2-HNP and NFL degradation over Ag_3PO_4@5 mLγ-G composite were provided in Fig. S4. The retention time of phenol, 2-HNP and NFL were 4.47, 3.64 and 3.96 min, respectively. It could be clearly seen that the intensity of characteristic peak decreased with the prolongation of illumination time, and finally disappeared completely. The above results fully demonstrated that the addition of γ-G could significantly improve the catalytic performance of Ag_3PO_4, which was mainly results from that γ-

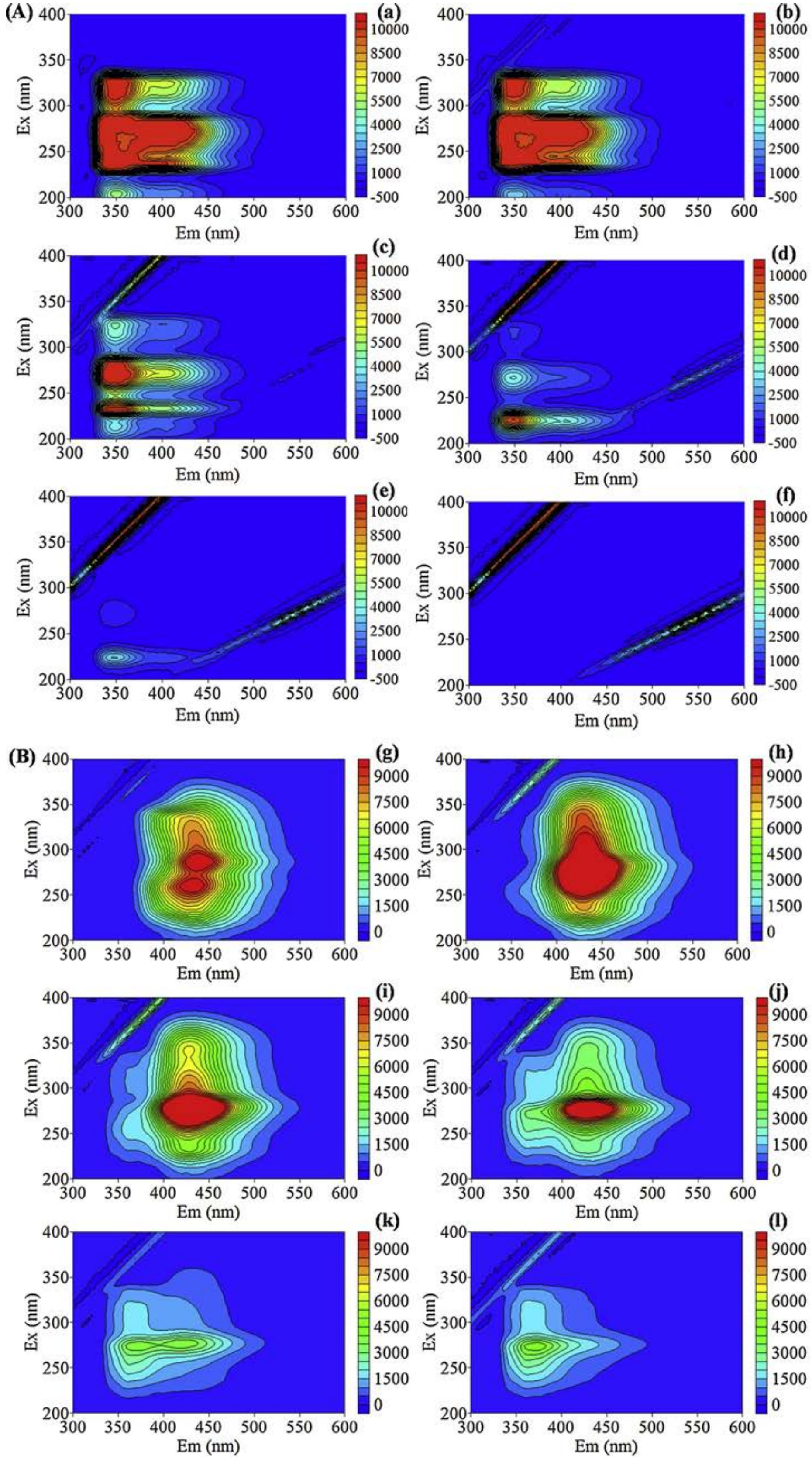

Fig. 9. (A) 3D EEMs of the 2-HNP (a), collected after 30 min adsorption in dark (b) and (c–f) obtained after an irradiation time of 1, 2, 3 and 5 min, respectively; (B) 3D EEMs of the NFL collected after 30 min adsorption in dark (g) and (h–l) obtained after an irradiation time of 1, 3, 5, 8 and 12 min, respectively.

G could serve as the photogenerated electrons transfer layer to rapidly transfer photogenerated electrons away from photogenerated holes. Efficient separation of photogenerated carriers produced more free radicals and photogenerated holes with the ability to oxidize and degrade pollutants molecules.

In order to explore the degradation process of pollutants, the reaction solution was determined by the 3D EEMs and LC–MS. The 2-HNP solution collected after adsorption reaction and at different irradiation time was detected by the 3D EEMs (Fig. 9A). As presented in Fig. 9a, three peaks of fluorescence signals located at 205/350 nm, 270/350 nm and 325/350 nm (Ex/Em) could be observed clearly, which were the typical signal peak of polycyclic aromatic hydrocarbons [51,52]. After 30 min of adsorption, the intensity of fluorescence signals almost did not decreased. However, the intensity of characteristic signal decreased significantly after 1 min of illumination, and there was no fluorescence signal could be detected after 5 min of irradiation. Interestingly, there were two new characteristic peaks (225/350 nm and 225/410 nm) appeared in the process of photocatalytic degradation, indicating the formation of degradation intermediates (Fig. 9c–f). Similarly, the reaction solution of NFL was also detected by 3D EEMs (Fig. 9 B). As shown in Fig. 9g, two peaks (at Ex/Em = 260/425 nm and 280/435 nm) could be found in the spectrum of NFL solution collected after 30 min adsorption in darkness. Surprisingly, after exposure to the visible light for 1 min, the intensity of the fluorescent signal did not weaken but increased, presenting as a strong signal peak (265/430 nm). During the illumination of $3-8$ min, the fluorescence signals gradually decreased with the reaction time (Fig. 9h–k). In particular, after 8 min of irradiation, the characteristic peaks disappeared and two new signal peaks appeared (275/375 nm and 275/415 nm) (Fig. 9k), indicating the degradation products were changed continuously with the extension of irradiation time. Finally, after 12 min of illumination, the signal peak was located at 275/375 nm (Fig. 9l), which may be the characteristic signal peak of small molecule acids [53–55].

In order to further explore the specific intermediates and degradation pathways, the LC–MS was performed. The MS spectra of NFL intermediates at different reaction time were provided in Fig. S5, the typical peak located at *m/z* 320 was identified as NFL molecule (Fig. S5a). The piperazinyl ring with high charge density was more susceptible to being attacked by the radicals and produced the intermediate with the *m/z* of 350 (Fig. S5b), which was coincided with the previous reported [56]. After the ring-opening and oxidation reactions on the piperazinyl ring, the intermediates (*m/z* = 322, 294, 279 and 261) were generated subsequently (Fig. S5d). The products with *m/z* of 279 and 261 continued to lose CO, resulting in the intermediate molecules with *m/z* of 251 and 233, respectively (Fig. S5e). Finally, these intermediates could be further oxidized by the active species into short-chain carboxylic acids (*m/z* = 229, 145 and 118) (Fig. S5h, i). Besides, another degradation pathway was also proposed, in which the fluorine connected to the quinolone ring was firstly substituted with a −OH group [57,58]. Accordingly, the products with protonated forms at *m/z* 318 generated (Fig. S5c), and followed with lose of −COOH, ring-opening, lose of −CO and C_2H_5N, which corresponded to the intermediate product with *m/z* of 274, 276, 248 and 205, respectively (Fig. S5f, g). Finally, these intermediates were further degraded into short-chain carboxylic acids (*m/z* = 160, 118 and 99). Based on the above analysis results, the schematic diagram of degradation pathway for NFL was summarized in Fig. 10a.

The degradation intermediates of 2-HNP was also determined by the LC-(-ESI) MS, and the MS spectra were presented in Fig. S6. The obvious mass signal (*m/z* = 143) corresponding to 2-HNP could be clearly observed (Fig. S6a). Since the hydroxyl groups in 2-HNP will activate the ortho-and para-hydrogen atoms on the benzene ring, these two reaction sites are vulnerable to attack and oxidation. The intermediate products with *m/z* 159, 195 and 173 were then generated (Fig. S6b–d). After the ring-opening and oxidation reaction, the products of *m/z* 165, 177 and 143 appeared subsequently. Then, the intermediates with *m/z* of 165

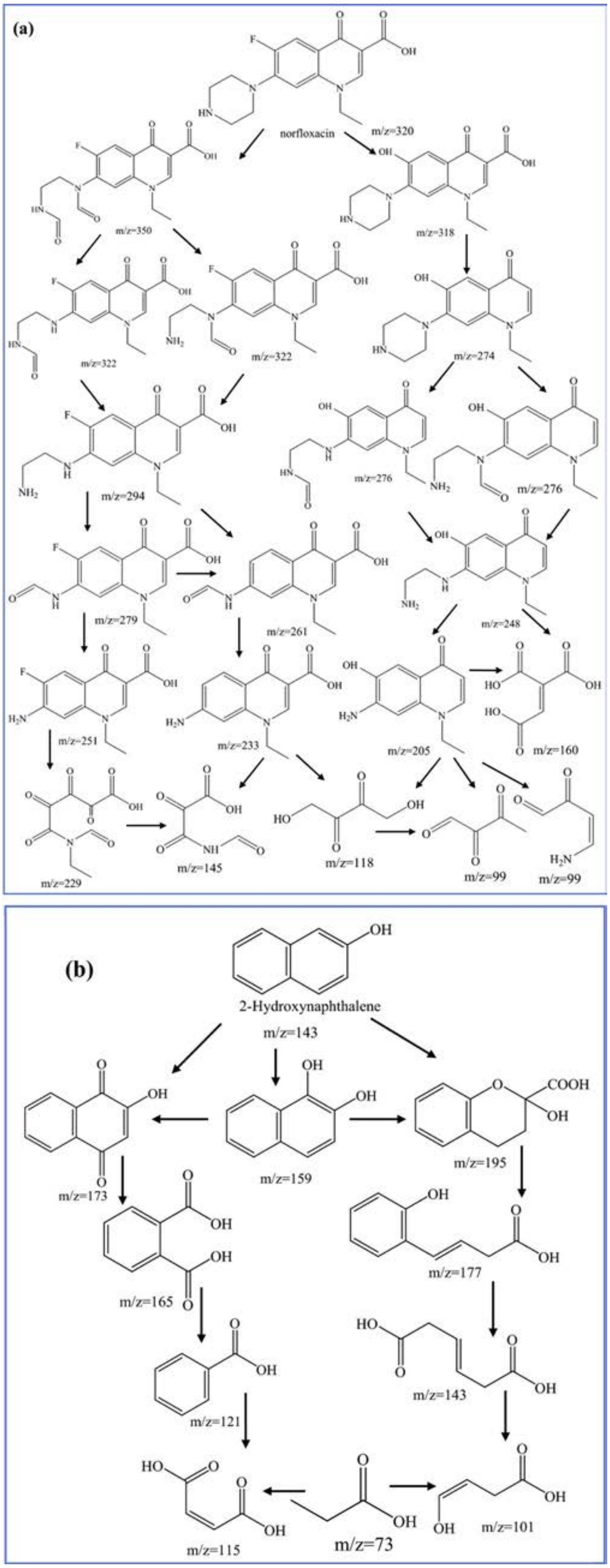

Fig. 10. A possible photocatalytic degradation pathway of NFL (a) and (b) 2-HNP.

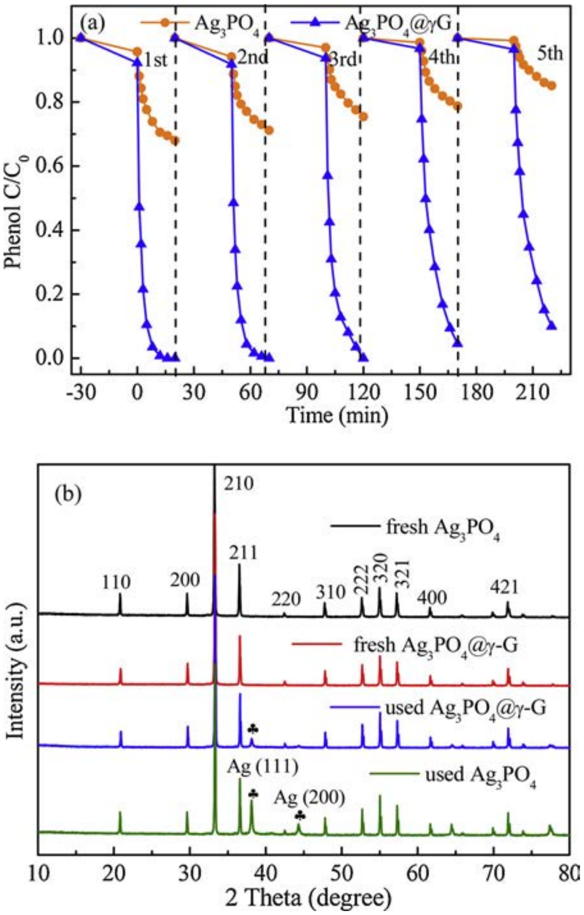

Fig. 11. Cycling test for the photocatalytic degradation of phenol in the presence of different samples (a); XRD patterns of the fresh and used photocatalysts (b).

further fragmented to the product with an m/z value of 121 by losing —COOH. Finally, the partial elimination reactions and further oxidation reaction occurred on the above intermediates, resulting in the formation of short-chain carboxylic acids (m/z = 115, 101 and 73). The possible degradation pathway was shown in Fig. 10b.

3.3. Photostability and recyclability

In order to evaluate the photostability of obtained photocatalysts, the cycling experiments of as-prepared Ag_3PO_4 and Ag_3PO_4@γ-G samples were carried out. Briefly, the used photocatalysts were collected after filtration, washing, drying and then applied to another round of phenol degradation under the same conditions. As shown in Fig. 11a, the photocatalytic activity of Ag_3PO_4 significantly declined after five cycles, and the removal rate of phenol decreased about 53.3 %. This was results from the photocorrosion of Ag_3PO_4 that reduction of Ag^+ into metallic Ag after exposure to irradiation. However, the Ag_3PO_4@γ-G sample still remained excellent photocatalytic performance after five cycles. It was worth mentioning that the removal rate of phenol could still reach 100 % after three cycles, and the degradation efficiency of 95.5 % and 90 % was also achieved after the fourth and fifth cycles, respectively. The above results indicated that the coupling of γ-G could significantly improve the photocatalytic activity and photostabilty of Ag_3PO_4. The γ-G could serve as the photogenerated electrons transfer layer to rapidly transfer photogenerated electrons to the catalyst surface, thus markedly inhibiting the reduction of Ag_3PO_4 into Ag^0 by photogenerated electrons and enhancing the photogenerated carrier separation efficiency.

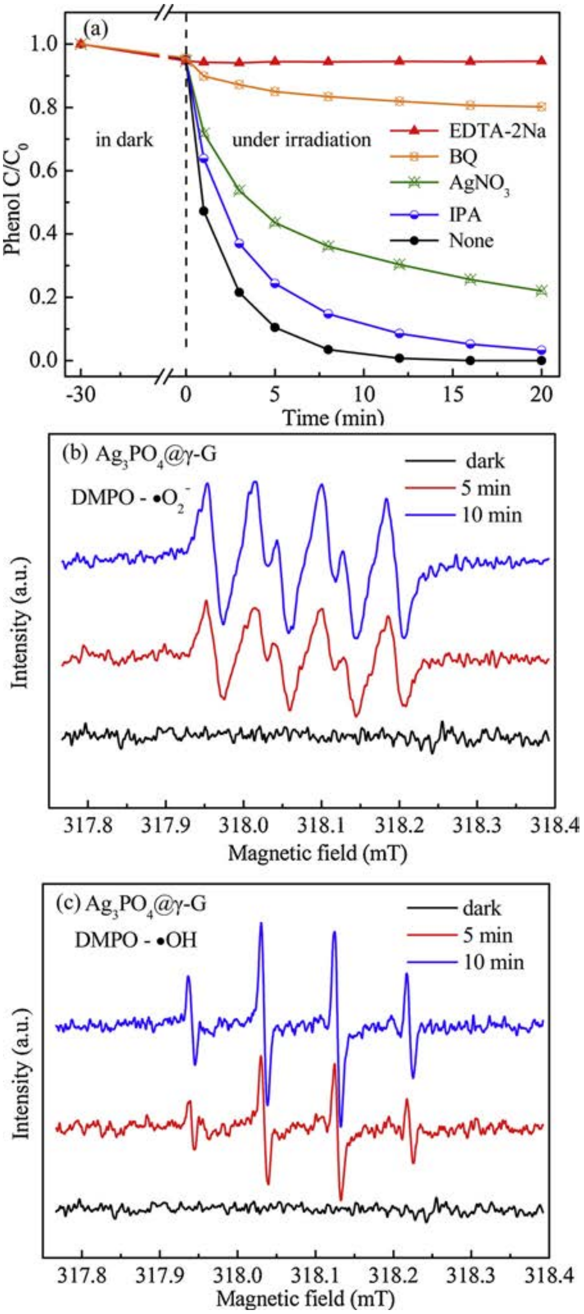

Fig. 12. (a) Photodegradation curves of phenol over Ag_3PO_4@γ-G composite with different active species scavengers. ESR spectra of radical adducts trapped by DMPO in the different samples dispersion under both the dark and visible light irradiation (λ > 420 nm) condition: (b) in methanol dispersion for DMPO-$^{\cdot}O_2^-$; (c) in aqueous dispersion for DMPO$^{\cdot}$OH.

The XRD pattern of recycled Ag_3PO_4 and Ag_3PO_4@γ-G were also measured to investigate its photostability, and the results were provided in Fig. 11b. In order to readily compare the peak strength of different samples, the XRD data were normalized. It could be clearly observed that the characteristic diffraction peaks ascribed to the Ag appeared in the XRD pattern of used Ag_3PO_4, and the peaks located at 38.12° and 44.28° correspond to the (111) and (200) plane of metallic Ag, respectively. The crystallization damage of Ag_3PO_4 and the massive accumulation of metallic Ag on the catalyst surface would decrease the photoactivity and light absorption efficiency of Ag_3PO_4. In contrast, there was just a weak diffraction peak at 38.12° could be found on the XRD pattern of the Ag_3PO_4@γ-G composite, indicating that only a small amount of Ag generated during the photodegradation process. Because the formation of charge transmission-bridge and the Schottky barriers at the metal-semiconductor interface, the presence of minor amount of Ag could accelerate the charge transfer rate and promote the separation of electron-hole pairs, which also contribute to the high catalytic activity of Ag_3PO_4@γ-G composite [17].

3.4. Possible photocatalytic mechanism of Ag_3PO_4@γ-G

3.4.1. Active species in photocatalytic reaction

In order to reveal the enhanced photocatalytic activity of Ag_3PO_4@γ-G composites and elucidate the intrinsic mechanism of organic pollutant degradation, the role of main active species were investigated. Different radical quenchers were added to the reaction system for radical trapping experiments [59,60]. The benzoquinone (BQ), ethylenediamine tetra acetic acid disodium salt (EDTA-2Na), isopropanol (IPA) and $AgNO_3$ were used as scavengers for superoxide radical, photogenerated holes, hydroxyl radicals and photogenerated electrons, respectively [61,62]. As shown in Fig. 12a, the phenol decomposition process was significantly inhibited with EDTA-2Na, indicating that the photogenerated holes played an important role in the photocatalytic reaction. Similarly, the addition of BQ also exhibited an extremely negative effect, suggesting that $^{\cdot}O_2^-$ radicals were another dominant active species during the reaction process. Relatively obvious decrease of photocatalytic activity could be found in the presence of $AgNO_3$, implying that the photogenerated electrons also worked in the photodegradation process. Compared with the other three scavengers, the photocatalytic activity of Ag_3PO_4@γ-G was the least reduced after the addition of IPA. It could deduce that holes, $^{\cdot}O_2^-$, photogenerated electrons and $^{\cdot}OH$ all worked in the photodegradation process, while $^{\cdot}O_2^-$ and holes primarily contributed to the photocatalytic performace enhancement. The results were good in agreement with the fact that the Ag_3PO_4 possess highly positive valence band position, in which most organic pollutants can be directly oxidized by the photogenerated holes. The ESR spin-trap with DMPO technique was performed to confirm the reactive oxygen species generated in the photocatalytic process of Ag_3PO_4@γ-G composite, and the results were provided in Fig. 12b. The typical signals ascribed to the DMPO-$^{\cdot}O_2^-$ and DMPO-$^{\cdot}OH$ could be clearly observed after exposure to the visible light irradiation, while no signal could be found in the darkness under identical conditions, which indicated that the $^{\cdot}O_2^-$ and $^{\cdot}OH$ produced successfully during the photocatalytic process. Moreover, the intensity of characteristic peaks increased apparently with the visible light irradiation time prolonging, suggesting the -$^{\cdot}O_2^-$ and $^{\cdot}OH$ could be produced continuously in the Ag_3PO_4@γ-G reaction system. The presence of a large number of radicals was contributed to the excellent photocatalytic performance of Ag_3PO_4@γ-G. The results of ESR were consistent with that of radical trapping experiments.

3.4.2. DFT calculations and charge transfer mechanism analysis

In order to further explore the photogenerated charge migration mechanism, the DFT calculations were thus performed. Firstly, the band structure of bulk Ag_3PO_4 was calculated based on the density functional theory and the GGA-PBE exchange-correlation functional for describing the interactions, the results were provided in Fig. 13a. It could be found that the direct band gap was 0.24 eV in G point and the indirect band gap between M and G was 0.19 eV, which obviously underestimated the band gap of Ag_3PO_4. Therefore, hybrid-DFT based on the hybrid functional HSE06 for describing the interactions was applied to calculate the band structure of bulk Ag_3PO_4. As shown in Fig. 13b, the direct band gap was 2.06 eV in G point and the indirect band gap between M and G was1.90 eV, the computation precision was increased greatly. Considering the experimental results, the hybrid DFT method is more suitable for the calculation of the electronic and band structures of Ag_3PO_4. Thus, the band structures of Ag_3PO_4@γ-G were calculated by the hybrid-DFT method, and the obtained results were used to calculate the band charge density. As shown in Fig. 13c, the highest occupied energy band (HOEB) was distributed on the Ag_3PO_4, which was mainly consisted by the O 2p orbital and Ag 4d orbital. However, for the lowest unoccupied energy band (LUEB), it was composed of the C 2p orbital in γ-G (Fig. 13d). Obviously, when the Ag_3PO_4@γ-G composite catalysts were exposed to the visible light, the electrons on HOEB could be excited to the LUEB, that is, the electrons on Ag_3PO_4 could be transferred rapidly to the γ-G. As a result, the photogenerated electrons and holes of Ag_3PO_4 were separated rapidly, leading to the great enhancement of carrier separation efficiency and significant improvement of photocatalytic performance. The excitation of electrons leaves photogenerated holes on HOEB, which can directly oxidize and decompose the pollutants.

The planar average electrostatic potential of Ag_3PO_4 (100) and Ag_3PO_4@γ-G in the z-direction was presented in Fig. 13e–f. The periodic lattice electrostatic potential could be clearly observed in the Ag_3PO_4 (100) (Fig. 13e). However, after the coupling with the γ-G, there was a significant decrease of potential near the γ-G sheet, indicating that a potential well was formed at the interfaces (Fig. 13f). The appearance of such a large built-in potential well could effectively hinder the recombination of photogenerated electron-hole pairs in the Ag_3PO_4@γ-G composite [63]. Combined with the results of band charge density analysis, it could be concluded that the photogenerated electrons of Ag_3PO_4 could be pumped to the γ-G sheets under the driving of the built-in potential in the composites [64].

The above results implied a large number of charge transferred between the different constituents after the coupling of γ-G, and it could be visualized by the three-dimensional charge density difference [65]. The charge density difference was calculated from the following equation:

$$\Delta\rho=\rho\, Ag_3PO_4(100)@\gamma G-\rho\, Ag_3PO_4(100)-\rho\,(\gamma G) \tag{1}$$

Where $\rho Ag_3PO_4(100)$@γ-G, $\rho Ag_3PO_4(100)$ and ρ (γ-G) are the charge density of the composite catalysts, $Ag_3PO_4(100)$ surface and γ-G in the same configuration, respectively. As shown in Fig. 13g, the charge redistribution mainly occurred at the $Ag_3PO_4(100)$@γ-G interface, and there was almost no charge transfer far away from the interface. Moreover, it could be clearly observed that there was a strong charge accumulation above the Ag atoms. While the regions of charge depletion appeared on the lower side of the γ-G which facing the interface and the upper side of Ag atoms in the top layer. Similar phenomena also have been reported, indicating the strong interaction between the interfaces of Ag_3PO_4 and γ-G [64]. The above calculation results indicated that γ-G can be served as an effective transfer layer of photogenerated electrons due to the intense interface interaction and the large built-in potential in the composite.

On the basis of the above experimental data and calculation analysis, a reasonable photocatalytic mechanism of Ag_3PO_4@γ-G composite was proposed, as presented in Fig. 14. According to the above results, the conduction band potential (E_{CB}) and valence band potential (E_{VB}) of Ag_3PO_4 were calculated as 0.44 and 2.79 eV, respectively. When exposed to the visible light, the electrons at the valence band (VB) of Ag_3PO_4 are easily excited to the conduction band (CB), and then the holes are formed in VB. The γ-G with high-velocity carrier transport capacity could serve as an effective transfer layer of photogenerated electrons. It rapidly transported electrons to the surface of the photocatalyst, and then reacted with water and oxygen to generate $^{\cdot}OH$ and -$^{\cdot}O_2^-$, which can oxidize organic pollutants. Moreover, the rapid migration of electrons on γ-G can efficiently keep electrons away from the photogenerated holes, thus significantly promoting the separation of photogenerated carriers and improving the photocatalytic performance of catalysts. Meanwhile, the photogenerated holes on the VB of Ag_3PO_4 possess strong oxidation capability because of its highly positive valence band position, which can directly attack, oxidize and decompose pollutants. The enhanced photocatalytic activity and anti-photocorrosion performance of Ag_3PO_4@γ-G can be attributed to the following

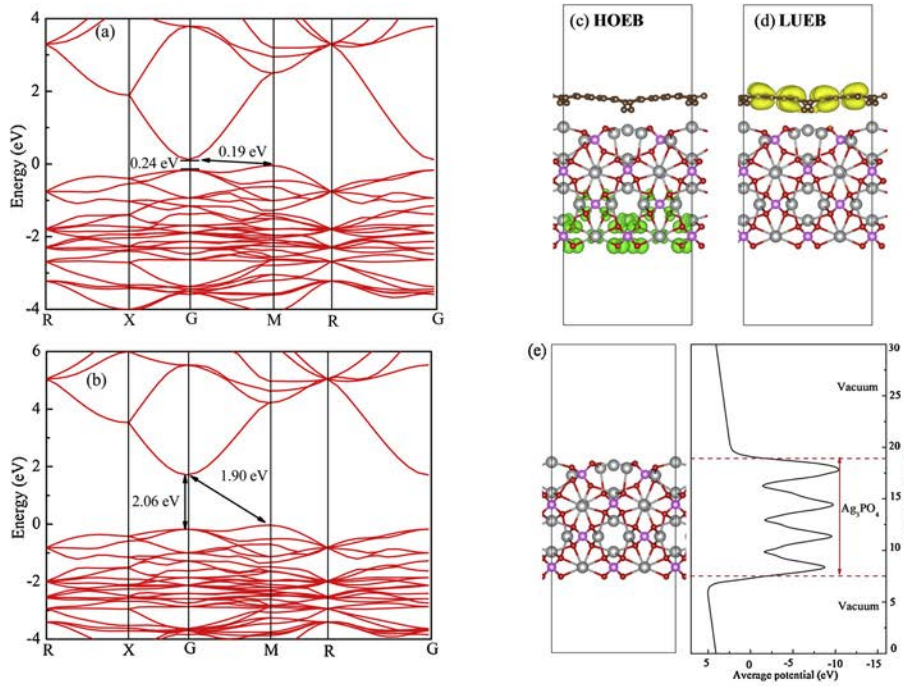

Fig. 13. Band structure of bulk Ag_3PO_4 calculated using the (a) standard DFT method and (b) the hybrid-DFT (hybrid functional HSE06); The band charge density distributions of (c) the highest occupied energy band (HOEB) and (d) the lowest unoccupied energy band (LUEB) with an isovalue of 0.0018 e/Å^3, the green and yellow colors represent the charge density distribution with and without electron occupation; Profile of the planar average electrostatic potential for (e) Ag_3PO_4(100) and (f) Ag_3PO_4@γ-G composite in the z-direction; (g) 3D charge density difference for the Ag_3PO_4@γ-G composite with an isovalue of 0.0008 e/Å^3, and the blue and green isosurfaces represent charge accumulation and depletion in the space. (For interpretation of the references to colour in this figure legend, the reader is referred to the web version of this article).

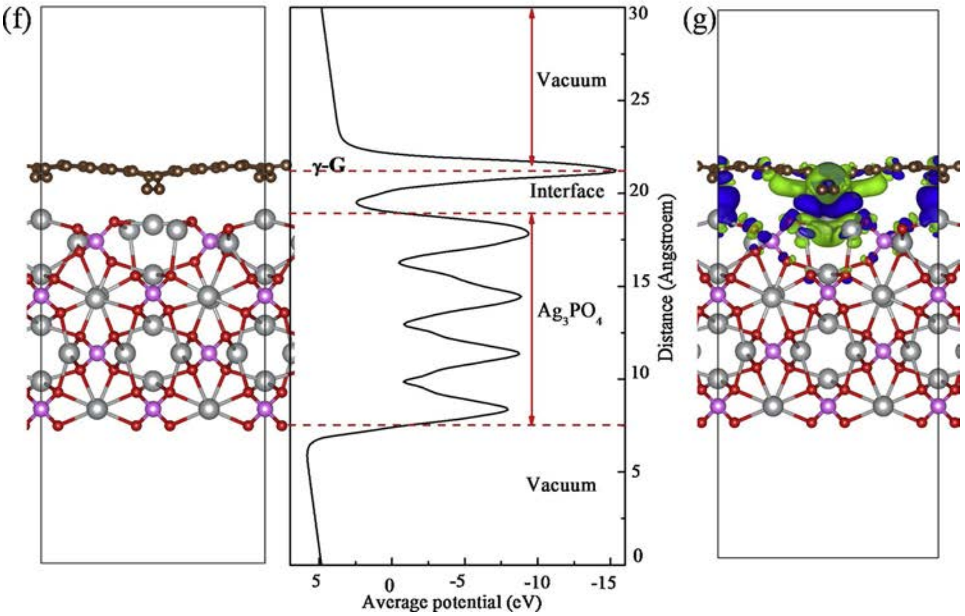

several reasons. Firstly, high electrical conductivity of γ-G facilitates it being an effective acceptor of the photogenerated electrons and promotes the transfer of electrons. Secondly, the sufficient interfacial contact and intense strong interaction are beneficial to carrier migration. Thirdly, the introduction of γ-G promotes the formation of a strong built-in electric field in the catalyst system, which makes the electron flow trapped by the electron transfer layer.

4. Conclusions

In summary, the novel Ag_3PO_4@γ-G composite photocatalysts were prepared by a facile preparation method combined the mechanochemistry and electrostatically driven self-assembly approach for the first time. The DFT calculation results of Ag_3PO_4@γ-G composite, including the band charge density distributions, planar average electrostatic potential and three-dimensional charge density difference, indicated that the successful construction of electrons transfer layer in composite catalyst. The introduction of γ-G as electrons transfer layer led to the excellent photocatalytic activities and photostability of Ag_3PO_4@γ-G composite photocatalysts. The removal efficiency of phenol, 2-HNP and NFL reached 100 %, only 16, 5 and 8 min were needed, respectively. The results of LC−MS and 3D EEMs showed that the 2-HNP and NFL mainly degraded into short-chain carboxylic acids. The results of free radical quenching experiment and ESR characterization suggested that all kinds of active species worked in the degradation process, while the photogenerated holes and superoxide radicals played a dominant role. In this study, an effective photocatalytic material was prepared for environmental remediation. The construction

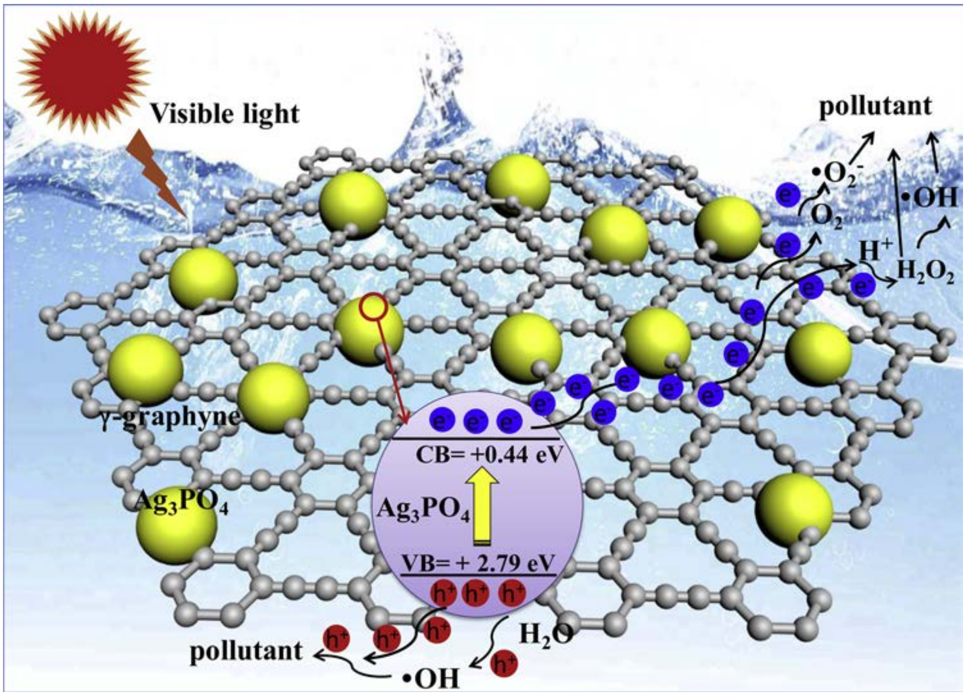

Fig. 14. Schematic illustration of photocatalytic mechanism for Ag_3PO_4@γ-G composite under visible light irradiation.

of electrons transfer layer with γ-G may provide a new strategy in the design of new catalyst with high efficient photocatalytic performance.

CRediT authorship contribution statement

Yan Lin: Conceptualization, Methodology, Investigation, Software, Writing - original draft. **Haiyang Liu:** Methodology, Data curation. **Chunping Yang:** Conceptualization, Supervision, Project administration, Funding acquisition. **Xin Wu:** Visualization, Investigation. **Cheng Du:** Conceptualization, Resources, Validation. **Limei Jiang:** Formal analysis, Writing - review & editing. **Yuanyuan Zhong:** Writing - review & editing.

Declaration of Competing Interest

The authors declare that they have no competing financial interests or personal relationships that could have appeared to influence the work reported in this paper.

Acknowledgments

Support from the National Natural Science Foundation of China (Grant No.: 51978178 and 51478172, 51521006), the Department of Science and Technology of Guangdong Province of China (Contract No.:2019A1515012044 and 2018S0011), the International S&T Cooperation Program of China (Contract No.: 2015DFG92750), the Natural Science Foundation of Zhejiang Province of China (Grant No.: LY17E080002), and the Department of Science and Technology of Hunan Province of China (Contract No.: 2017JJ2029 and 2017SK2362) is highly appreciated.

Appendix A. Supplementary data

Supplementary material related to this article can be found, in the online version, at doi:https://doi.org/10.1016/j.apcatb.2019.118479.

References

[1] D. Shindell, C.J. Smith, Climate and air-quality benefits of a realistic phase-out of fossil fuels, Nature 573 (2019) 408–411.
[2] H. Yamashita, K. Mori, Y. Kuwahara, T. Kamegawa, M. Wen, P. Verma, M. Che, Single-site and nano-confined photocatalysts designed in porous materials for environmental uses and solar fuels, Chem. Soc. Rev. 47 (2018) 8072–8096.
[3] T. Kamegawa, Y. Ishiguro, H. Yamashita, Photocatalytic properties of TiO_2-loaded porous silica with hierarchical macroporous and mesoporous architectures in the degradation of gaseous organic molecules, Catal. Today 332 (2019) 222–226.
[4] Z.J. Zhang, Y.F. Zhu, X.J. Chen, H.J. Zhang, J. Wang, A full-spectrum metal-free porphyrin supramolecular photocatalyst for dual functions of highly efficient hydrogen and oxygen evolution, Adv. Mater. 31 (2019) 1806626.
[5] H.W. Tian, M. Liu, W.T. Zheng, Constructing 2D graphitic carbon nitride nanosheets/layered MoS_2/graphene ternary nanojunction with enhanced photocatalytic activity, Appl. Catal. B: Environ. 225 (2018) 468–476.
[6] Z. Wei, M.L. Liu, Z.J. Zhang, W.Q. Yao, H.W. Tan, Y.F. Zhu, Efficient visible-light-driven selective oxygen reduction to hydrogen peroxide by oxygen-enriched graphitic carbon nitride polymers, Energy Environ. Sci. 11 (2018) 2581–2589.
[7] H.L. Yin, X.F. Chen, G.Y. Li, Y.D. Chen, W.J. Wang, T.C. An, P.K. Wong, H.J. Zhao, Sub-lethal photocatalysis bactericidal technology cause longer persistence of antibiotic-resistance mutant and plasmid through the mechanism of reduced fitness cost, Appl. Catal. B: Environ. 245 (2019) 698–705.
[8] H.W. Tian, K. Shen, X.Y. Hu, L. Qiao, W.T. Zheng, N, S co-doped graphene quantum dots-graphene-TiO_2 nanotubes composite with enhanced photocatalytic activity, J. Alloys Compd. 691 (2017) 369–377.
[9] D.J. Martin, G.G. Liu, S.J. Moniz, Y. Bi, A.M. Beale, J.H. Ye, J.W. Tang, Efficient visible driven photocatalyst, silver phosphate: Performance, understanding and perspective, Chem. Soc. Rev. 44 (2015) 7808–7828.
[10] Y.P. Bi, S.X. Ouyang, N. Umezawa, J.Y. Cao, J.H. Ye, Facet effect of single-crystalline Ag_3PO_4 sub-microcrystals on photocatalytic properties, J. Am. Chem. Soc. 133 (2011) 6490–6492.
[11] X. Guan, L. Guo, Cocatalytic effect of $SrTiO_3$ on Ag_3PO_4 toward enhanced photocatalytic water oxidation, ACS Catal. 4 (2014) 3020–3026.
[12] C.T. Dinh, T.D. Nguyen, F. Kleitz, T.O. Do, Large-scale synthesis of uniform silver orthophosphate colloidal nanocrystals exhibiting high visible light photocatalytic activity, Chem. Commun. 47 (2011) 7797–7799.
[13] Y. Lin, S.H. Wu, C.P. Yang, M. Chen, X. Li, Preparation of size-controlled silver phosphate catalysts and their enhanced photocatalysis performance via synergetic effect with MWCNTs and PANI, Appl. Catal. B: Environ. 245 (2019) 71–86.
[14] Y.P. Bi, H.Y. Hu, Z.B. Jiao, H.C. Yu, G.X. Lu, J.H. Ye, Two-dimensional dendritic Ag_3PO_4 nanostructures and their photocatalytic properties, Phys. Chem. Chem. Phys. 14 (2012) 14486–14488.
[15] J.J. Guo, S.X. Ouyang, H. Zhou, T. Kako, J.H. Ye, $Ag_3PO_4/In(OH)_3$ composite photocatalysts with adjustable surface-electric property for efficient photodegradation of organic dyes under simulated solar-light irradiation, J. Phys. Chem. C 117 (2013) 17716–17724.
[16] X.J. Chen, Y.Z. Dai, X.Y. Wang, Methods and mechanism for improvement of photocatalytic activity and stability of Ag_3PO_4: a review, J. Alloys Compd. 649

(2015) 910–932.

[17] Y.P. Liu, L. Fang, H.D. Lu, Y.W. Li, C.Z. Hu, H.Y. Yu, One-pot pyridine-assisted synthesis of visible-light-driven photocatalyst Ag/Ag_3PO_4, Appl. Catal. B: Environ. 115–116 (2012) 245–252.

[18] Y.Y. Bu, Z.Y. Chen, C. Sun, Highly efficient Z-Scheme Ag_3PO_4/Ag/WO_{3-x} photocatalyst for its enhanced photocatalytic performance, Appl. Catal. B: Environ. 179 (2015) 363–371.

[19] L. Liu, L. Ding, Y.G. Liu, W.J. An, S.L. Lin, Y.H. Liang, W.Q. Cui, A stable Ag_3PO_4@PANI core@shell hybrid: Enrichment photocatalytic degradation with π-π conjugation, Appl. Catal. B: Environ. 201 (2017) 92–104.

[20] X.F. Yang, H.Y. Cui, Y. Li, J.L. Qin, R.X. Zhang, H. Tang, Fabrication of Ag_3PO_4-Graphene composites with highly efficient and stable visible light photocatalytic performance, ACS Catal. 3 (2013) 363–369.

[21] H.C. Zhang, H. Huang, H. Ming, H.T. Li, L.L. Zhang, Y. Liu, Z.H. Kang, Carbon quantum dots/Ag_3PO_4 complex photocatalysts with enhanced photocatalytic activity and stability under visible light, J. Mater. Chem. 22 (2012) 10501–10506.

[22] Y. Lin, S.H. Wu, X. Li, X. Wu, C.P. Yang, G.M. Zeng, Y.R. Peng, Q. Zhou, L. Lu, Microstructure and performance of Z-scheme photocatalyst of silver phosphate modified by MWCNTs and Cr-doped $SrTiO_3$ for malachite green degradation, Appl. Catal. B: Environ. 227 (2018) 557–570.

[23] Y. Lin, X. Wu, Y. Han, C.P. Yang, Y. Ma, C. Du, Q. Teng, H.Y. Liu, Y.Y. Zhong, Spatial separation of photogenerated carriers and enhanced photocatalytic performance on Ag_3PO_4 catalysts via coupling with PPy and MWCNTs, Appl. Catal. B: Environ. 258 (2019) 117969.

[24] C.S. Huang, Y.J. Li, N. Wang, Y.R. Xue, Z.C. Zuo, H.B. Liu, Y.L. Li, Progress in research into 2D graphdiyne-based materials, Chem. Rev. 118 (2018) 7744–7803.

[25] Q.D. Li, Y. Li, Y. Chen, L.L. Wu, C.F. Yang, X.L. Cui, Synthesis of γ-graphyne by mechanochemistry and its electronic structure, Carbon 136 (2018) 248–254.

[26] H. Shang, Z. Zuo, L. Li, F. Wang, H. Liu, Y. Li, Y. Li, Ultrathin graphdiyne nanosheets grown in situ on copper nanowires and their performance as Lithium-ion battery anodes, Angew. Chem. Int. Ed. 57 (2018) 774–778.

[27] G.X. Li, Y.L. Li, H.B. Liu, Y.B. Guo, Y.J. Li, D.B. Zhu, Architecture of graphdiyne nanoscale films, Chem. Commun. 46 (2010) 3256–3258.

[28] L. Wu, Q. Li, C. Yang, X. Ma, Z. Zhang, X. Cui, Constructing a novel TiO_2/γ-graphyne heterojunction for enhanced photocatalytic hydrogen evolution, J. Mater. Chem. A 6 (2018) 20947–20955.

[29] A.R. Puigdollers, G. Alonso, P. Gamallo, First-principles study of structural, elastic and electronic properties of α-, β- and γ-graphyne, Carbon 96 (2016) 879–887.

[30] Photocatalytic properties of graphdiyne and graphene modified TiO_2: From theory to experiment, ACS Nano 7 (2013) 1504–1512.

[31] Y.J. Li, Q.N. Liu, W.F. Li, H. Meng, Y.Z. Lu, C.X. Li, Synthesis and supercapacitor application of alkynyl carbon materials derived from CaC_2 and polyhalogenated hydrocarbons by interfacial mechanochemical reactions, ACS Appl. Mater. Interfaces 9 (2017) 3895–3901.

[32] M. Turberg, K.J. Ardila-Fierro, C. Bolm, J.G. Hernandez, Altering copper-catalyzed A^3couplings by mechanochemistry: one-pot synthesis of 1,4-diamino-2-butynes from aldehydes, amines, and calcium carbide, Angew. Chem. Int. Ed. 57 (2018) 10718–10722.

[33] C.F. Yang, Y. Li, Y. Chen, Q.D. Li, L.L. Wu, X.L. Cui, Mechanochemical synthesis of γ-graphyne with enhanced lithium storage performance, Small 15 (2019) 1804710.

[34] Q.D. Li, C.F. Yang, L.L. Wu, H. Wang, X.L. Cui, Converting benzene into γ-graphyne and its enhanced electrochemical oxygen evolution performance, J. Mater. Chem. A 7 (2019) 5981–5990.

[35] C. Li, X.L. Lu, Y.Y. Han, S.F. Tang, Y. Ding, R.R. Liu, H.H. Bao, Y.L. Li, J. Luo, T.B. Lu, Direct imaging and determination of the crystal structure of six-layered graphdiyne, Nano Res. 11 (2018) 1714–1721.

[36] R. Matsuoka, R. Sakamoto, K. Hoshiko, S. Sasaki, H. Masunaga, K. Nagashio, H. Nishihara, Crystalline graphdiyne nanosheets produced at a gas/liquid or liquid/liquid interface, J. Am. Chem. Soc. 139 (2017) 3145–3152.

[37] J.Y. Zhou, X. Gao, R. Liu, Z.Q. Xie, J. Yang, S.Q. Zhang, G.M. Zhang, H.B. Liu, Y.L. Li, J. Zhang, Z.F. Liu, Synthesis of graphdiyne nanowalls using acetylenic coupling reaction, J. Am. Chem. Soc. 137 (2015) 7596–7599.

[38] J. Li, X. Gao, B. Liu, Q.L. Feng, X.B. Li, M.Y. Huang, Z.F. Liu, J. Zhang, C.H. Tung, L.Z. Wu, Graphdiyne: a metal-free material as hole transfer layer to fabricate quantum dot-sensitized photocathodes for hydrogen production, J. Am. Chem. Soc. 138 (2016) 3954–3957.

[39] H. Du, Z. Zhang, J. He, Z. Cui, J. Chai, J. Ma, Z. Yang, C. Huang, G. Cui, A delicately designed sulfide graphdiyne compatible cathode for high-performance lithium/magnesium-sulfur batteries, Small 13 (2017) 1702277.

[40] J. Zwara, E. Grabowska, T. Klimczuk, W. Lisowski, A. Zaleska-Medynska, Shape-dependent enhanced photocatalytic effect under visible light of Ag_3PO_4 particles, J. Photochem. Photobiol. A 367 (2018) 240–252.

[41] Z.C. Zhuang, Y. Li, Z.L. Li, F. Lv, Z.Q. Lang, K.N. Zhao, L. Zhou, L. Moskaleva, S.J. Guo, L.Q. Mai, MoB/g-C_3N_4 interface materials as a schottky catalyst to boost hydrogen evolution, Angew. Chem. Int. Ed. 57 (2018) 496–500.

[42] C.Y. Feng, Y.C. Deng, L. Tang, G.M. Zeng, J.J. Wang, J.F. Yu, Y.N. Liu, B. Peng, H.P. Feng, J.J. Wang, Core-shell Ag_2CrO_4/N-GQDs@g-C_3N_4 composites with anti-photocorrosion performance for enhanced full-spectrum-light photocatalytic activities, Appl. Catal. B: Environ. 239 (2018) 525–536.

[43] H. Guo, C.G. Niu, L. Zhang, X.J. Wen, C. Liang, X.G. Zhang, D.L. Guan, N. Tang, G.M. Zeng, Construction of direct Z-Scheme AgI/$Bi_2Sn_2O_7$ nanojunction system with enhanced photocatalytic activity: Accelerated interfacial charge transfer induced efficient Cr(VI) reduction, tetracycline degradation and *Escherichia coli* inactivation, ACS Sustain. Chem. Eng. 6 (6) (2018) 8003–8018.

[44] Y. Zhou, X.J. Zhang, Q. Zhang, F. Dong, F. Wang, Z. Xiong, Role of graphene on the band structure and interfacial interaction of Bi_2WO_6/graphene composites with enhanced photocatalytic oxidation of NO, J. Mater. Chem. A 2 (2014) 16623–16631.

[45] Z.J. Sun, H.F. Zheng, J.S. Li, P.W. Du, Extraordinarily efficient photocatalytic hydrogen evolution in water using semiconductor nanorods integrated with crystalline Ni_2P cocatalysts, Energy Environ. Sci. 8 (2015) 2668–2676.

[46] C.M. Li, Y.H. Du, D.P. Wang, S.M. Yin, W.G. Tu, Z. Chen, M. Kraft, G. Chen, R. Xu, Unique P-Co-N surface bonding states constructed on g-C_3N_4 nanosheets for drastically enhanced photocatalytic activity of H_2 evolution, Adv. Funct. Mater. 27 (2017) 1604328.

[47] Y. Yang, Z.T. Zeng, G.M. Zeng, D.L. Huang, R. Xiao, C. Zhang, C.Y. Zhou, W.P. Xiong, W.J. Wang, M. Cheng, W.J. Xue, H. Guo, X. Tang, D.H. He, Ti_3C_2 Mxene/porous g-C_3N_4 interfacial schottky junction for boosting spatial charge separation in photocatalytic H_2O_2 production, Appl. Catal. B: Environ. 258 (2019) 117956.

[48] S.L. Zhou, S.A. Zhang, F. Liu, J.J. Liu, J.J. Xue, D.J. Yang, C.T. Chang, ZnO nanoflowers photocatalysis of norfloxacin: Effect of triangular silver nanoplates and water matrix on degradation rates, J. Photochem. Photobiol. A 328 (2016) 97–104.

[49] Z.Y. Bai, Q. Yang, J.L. Wang, Catalytic ozonation of sulfamethazine using $Ce_{0.1}Fe_{0.9}OOH$ as catalyst: Mineralization and catalytic mechanisms, Chem. Eng. J. 300 (2016) 169–176.

[50] C. Liu, Y. Min, A.Y. Zhang, Y. Si, J.J. Chen, H.Q. Yu, Electrochemical treatment of phenol-containing wastewater by facet-tailored TiO_2: efficiency, characteristics and mechanisms, Water Res. 165 (2019) 114980.

[51] K. Vatsavai, H.C. Goicoechea, A.D. Campiglia, Direct quantification of monohydroxy-polycyclic aromatic hydrocarbons in synthetic urine samples via solid-phase extraction-room-temperature fluorescence excitation-emission matrix spectroscopy, Anal. Biochem. 376 (2008) 213–220.

[52] H. Wu, H.Y. Liu, Y. Lin, C.P. Yang, W. Lou, J.T. Sun, C. Du, D.M. Zhang, L.J. Nie, K. Yin, Y.Y. Zhong, Insights into mechanisms of UV/ferrate(VI) oxidation for degradation of phenolic pollutants: Role of superoxide radicals, Chemosphere (2020), https://doi.org/10.1016/j.chemosphere.2019.125490.

[53] Q. Zhou, X. Li, Y. Lin, C.P. Yang, W.C. Tang, S.H. Wu, D.H. Li, W. Lou, Effects of copper ions on removal of nutrients from swine wastewater and on release of dissolved organic matter in duckweed systems, Water Res. 158 (2019) 171–181.

[54] H. Hu, Q. Zhou, X. Li, W. Lou, C. Du, Q. Teng, D.M. Zhang, H.Y. Liu, Y.Y. Zhong, C.P. Yang, Phytoremediation of anaerobically digested swine wastewater contaminated by oxytetracycline via*Lemna aequinoctialis*: Nutrient removal, growth characteristics and degradation pathways, Bioresour. Technol. 291 (2019) 121853.

[55] S.H. Wu, Y. Lin, C.P. Yang, C. Du, Q. Teng, Y. Ma, D.M. Zhang, L.J. Nie, Y.Y. Zhong, Enhanced activation of peroxymonosulfate by $LaFeO_3$ perovskite supported on Al_2O_3 for degradation of organic pollutants, Chemosphere 237 (2019) 124478.

[56] H.B. Li, J. Chen, H.J. Hou, H. Pan, X.X. Ma, J.K. Yang, L.L. Wang, J.C. Crittenden, Sustained molecular oxygen activation by solid iron doped silicon carbide under microwave irradiation: mechanism and application to norfloxacin degradation, Water Res. 126 (2017) 274–284.

[57] D.H. Ding, C. Liu, Y.F. Ji, Q. Yang, L.L. Chen, C.L. Jiang, T.M. Cai, Mechanism insight of degradation of norfloxacin by magnetite nanoparticles activated persulfate: Identification of radicals and degradation pathway, Chem. Eng. J. 308 (2017) 330–339.

[58] C.P. Yang, H. Qian, X. Li, Y. Cheng, H.J. He, G.M. Zeng, J. Xi, Simultaneous removal of multicomponent VOCs in biofilters, Trends Biotechnol. 36 (2018) 673–685.

[59] J.L. Wang, L.J. Xu, Advanced oxidation processes for wastewater treatment: formation of hydroxyl radical and application, Crit. Rev. Env. Sci. Tec. 42 (2012) 251–325.

[60] S.H. Wu, H.J. He, L. Xiang, C.P. Yang, G.M. Zeng, B. Wu, S.Y. He, L. Li, Insights into atrazine degradation by persulfate activation using composite of nanoscale zero-valent iron and graphene: performances and mechanisms, Chem. Eng. J. 341 (2018) 126–136.

[61] L. Tang, C.Y. Feng, Y.C. Deng, G.M. Zeng, J.J. Wang, Y.N. Liu, H.P. Feng, J.J. Wang, Enhanced photocatalytic activity of ternary Ag/g-C_3N_4/$NaTaO_3$photocatalysts under wide spectrum light radiation: the high potential band protection mechanism, Appl. Catal. B: Environ. 230 (2018) 102–114.

[62] S.H. Wu, H.R. Li, X. Li, H.J. He, C.P. Yang, Performances and mechanisms of efficient degradation of atrazine using peroxymonosulfate and ferrate as oxidants, Chem. Eng. J. 353 (2018) 533–541.

[63] Y. Si, H.Y. Wu, H.M. Yang, W.Q. Huang, K. Yang, P. Peng, G.F. Huang, Dramatically enhanced visible light response of monolayer ZrS_2 via non-covalent modification by double-ring tubular B_{20} Cluster, Nanoscale Res. Lett. 11 (2016) 495.

[64] C.N. He, W.Q. Huang, L. Xu, Y.C. Yang, B.X. Zhou, G.F. Huang, P. Peng, W.M. Liu, Tuning near-gap electronic structure, interface charge transfer and visible light response of hybrid doped graphene and Ag_3PO_4 composite: dopant effects, Sci. Rep. 6 (2016) 22267.

[65] Y. Si, H.M. Yang, H.Y. Wu, W.Q. Huang, K. Yang, P. Peng, G.F. Huang, Tuning the near-gap electronic structure of Cu_2O by anion-cation co-doping for enhanced solar energy conversion, Mod. Phys. Lett. B 31 (2017) 1650429.